The effects of Be doping on the structure of Ga and Au-assisted GaAs-based heterostructured semiconductor nanowires.

Effekten av Be-doping på strukturen av Ga og
Au-assistert GaAs-baserte heterostructured
halvledere nanotråder.

Sethulakshmy Jayakumari

Master Thesis in Physics

FY3900

The effects of Be doping on the structure of Ga and Au-assisted GaAs-based heterostructured semiconductor nanowires.

Effekten av Be-doping på strukturen av Ga og Au-assistert GaAs-baserte heterostructured halvledere nanotråder.

Sethulakshmy Jayakumari

Trondheim 22-May-2013

ATJ van Helvoort (*Responsible supervisor*) IFY

Dheeraj Dasa (*Co-supervisor*) IET

Mazid Munshi (*Co-supervisor*) IET

Front cover image: Selected area diffraction pattern taken using Transmission electron microscope-Philips CM30, from the bottom part of high Be doped-Au-assisted GaAs nanowire (NW batch II As 605-2).

Abstract

The crystal structures of Gallium Arsenide (GaAs) based heterostructured semiconductor nanowires (NW) doped by different beryllium (Be) concentration grown by molecular beam epitaxy were characterized with the help of transmission electron microscopy techniques. Transmission electron microscopy (TEM) is a good tool to get a detailed set of crystallographic information from each nanowire batches. Two batches of nanowires are with different Be concentration, gold (Au) assisted, grown on GaAs substrate and the next two batches with different Be concentration, Gallium (Ga) assisted, grown on Silicon substrate were characterized. In addition to this, nanowire substrate interface were characterized, since sample preparation for TEM was a challenging experience. Four batches of nanowires were compared and analyzed. Doping concentration of Be affects the nanowire morphology and crystal structure. In Au assisted nanowires with low Be concentration are rod shaped nanowires. Whereas the nanowire batch with high Be seems to be tapered in morphology on the nanowire side facets and the crystal structure in both batches are zinc blende (ZB). Interestingly the Au-catalyzed highly doped nanowires have high density of stacking faults in which randomly distributed twins and periodic twinning or twinning super lattice were observed The next two NW batches are self-catalyzed and low doped Be has rod shaped in morphology and the one with highly doped Be tend to develop different nanowire morphology with respect to each other. The crystal structures in these two batches are also zinc blende (ZB). In general, Be was found to be incorporated even though the Be doping concentration is high or low in all the four nanowire batches. Compared with all the four NW batches, Be has a tendency to form ZB crystal structure. This investigation contribute to the understanding of incorporation of Be in nanowires, so that in future the knowledge helps to determine strategies on how to control the crystal defects and crystal phases of nanowires, for the application of optoelectronic nanowire based devices.

Acknowledgement

Contents

List of Abbreviations

BF   Bright-field

CCD   Charge-coupled device

DF   Dark-field

FCC   Face centered cubic

HCP   Hexagonal close packed

LED   Light emitting diodes

MBE   Molecular beam epitaxy

ML   Monolayer

NW   Nanowire

RHEED   Reflection high energy electron diffraction

SAD   Selected area diffraction

SFs   Stacking faults

TEM   Transmission electron microscopy

TSL   Twinning super lattice

VLS   Vapour-Liquid-Solid

WZ   Wurtzite

ZB   Zinc blende

Chapter 1

Introduction and motivation

Nanowires (NW) have the potential to be used in devices such as single electron memories, solar cells, light emitting diodes, lasers and single-molecule sensors. For solar cell applications semiconductor NWs are used as solar cell materials which have a great potential to reduce cost and to improve the efficiency of solar cell device. To build these NW based devices requires a great degree of control of the crystal structure and doping. Although NWs typically exhibit few crystal defects, nanowires made from III-V materials (for example, GaAs, GaP, InP and InAs) often show randomly distributed rotational twin planes and stacking faults [1]. Despite extensive works in the field of semiconductor nanowires, their electrical doping- a prerequisite for the fabrication of devices still remains an important field of research. The presence of dopants in the vapour phase may impede the nanowire formation or change the morphology of the nanowires [2].

TEM is a very good tool for the structural analysis of nano objects such as NWs and the crystal structure, growth direction, crystal defects etc can be characterized. The common TEM techniques such as bright field (BF), dark field (DF) and selected area diffraction (SAD) have been carried out for the detailed description of NW structure and crystal plane stacking sequence. In this study, the aim is to characterize the morphology and crystal structure of Be doped GaAs nanowires grown by molecular beam epitaxy. To get NW devices, have to realize control doping (low and high) with keeping control on crystal phase, defect density and morphology. Here in this study we focused on both Au catalyzed and Ga catalyzed NWs are studied and in addition to the growth on the substrate surfaces, NW substrate-interface on GaAs (111)B and Si(111) respectively are studied and compared by TEM. The effect of doping on the crystal structure and morphology can affect NW-device manufacturing and hence this has to be studied. The main aim of this study is to understand the formation of these crystal phases and defects and the ways to minimize the defect density and purify the crystal phases.

This fundamental study will be useful for the further future of NW growth optimization and design of new NW heterostructures for different electronic device applications. Initial part of my master project has been spent on practicing and learning the basics operations in TEM and learning crystallography for III-V NWs.

Chapter 2

Theory

Crystallography and Diffractometry of materials.

2.1 Crystals and crystal structure

The idea of the shape of the crystals was made by Johannes kepler in 1611 from the beautiful hexagonal patterns of snowflakes. Later in1665, Robert Hooke suggested that crystals occur in different shapes such as trapezia, rhombs, hexagons etc [3]. Discovery of X-ray diffraction for crystal analyses by Laue and his coworkers was a major turning-point in the advancement of solid state physics. In crystalline solids atoms or ions are regularly arranged whereas in non-crystalline or amorphous solids this regular order is missing. We can understand the structure of solids in terms of lattice and basis. Each lattice points contain an atom or a group of atoms or ions called basis. A crystal structure is a combination of lattice with basis [4].

Lattice is a regular periodic arrangement of atoms in space and apparently each lattice point will have identical surroundings. When the lattice points have identical surroundings we can connect any two lattice points with the help of translational vector t

In three dimension, $t = ua + vb + wc$……………………………….. (1)

where a, b, c are primitive translational vectors and u, v, w are integers and α, β, γ are the angles between the basis vectors, where α is the angle between b and c ,β the angle between a and c and γ the angle between a and b. Therefore { $a, b, c, \gamma, \beta, \gamma$} are called the lattice parameters of the unit cell and can be used to classify the seven crystal systems. A unit cell is the smallest building block of a crystal, which consists of atoms, molecules, or ions, whose geometrical arrangement determines the crystal's characteristic symmetry and

whose periodicity in space produces a crystal lattice. The position of the atom inside the unit cell is represented by position vector r is:

$$r = xa + yb + zc \dots\dots\dots\dots\dots\dots\dots\dots\dots\dots\dots\dots\dots\dots\dots\dots\dots \text{(2)}$$

In 1848, Bravais demonstrated that we can arrange lattice points of crystals in 14 different ways due to the different translational symmetrical operations in crystals such as rotation, reflection, inversion or a combination of these. There are basically seven crystal systems in three dimensions and some crystal system contains subclasses, in general there are 14 lattice types .Table 1 shows the seven crystal systems, their corresponding Bravais lattices and their properties.

Table (1): *The seven crystal systems, their corresponding Bravais lattices and properties.*[3]

System	Bravais lattices	Axial lengths	Angles
Cubic	PIF	a=b=c	$\alpha=\beta=\gamma=90^0$
Tetragonal	PI	a=b≠c	$\alpha=\beta=\gamma=90^0$
Orthorhombic	PICF	a≠b≠c	$\alpha=\beta=\gamma=90^0$
Trigonal	PR	a=b=c	$\alpha=\beta=\gamma\neq90^0$
Hexagonal	P	a=b≠c	$\alpha=\beta=90^0,\gamma=120^0$
Monoclinic	PC	a≠b≠c	$\alpha=\gamma=90^0,\beta\geq90^0$
Triclinic	P	a≠b≠c	$\alpha\neq\beta\neq\gamma=90^0$

Among these fourteen lattices, commonly seen materials for making devices are of cubic or hexagonal lattice type. Cubic lattices are of three types they are simple cubic (sc), body centered cubic (bcc) and face centered cubic (fcc). In sc the lattice points are at the eight corners of a cube, in bcc in addition to the eight lattice points at the corners there is one more lattice point at the center of the cube and in fcc there are lattice points in eight corners and additional lattice points in the center of each square faces. There are two types of atomic close packed arrangements in crystals they are hexagonal close packed (hcp) structure and cubic close packed (ccp) structure. In hcp basically there are two layers of atoms A and B, the atoms are stacked such a way that the first layer is A, second layer is B,

third layer is again goes directly above the first layer A, fourth layer goes over the second B layer and so on. This forms a stacking sequence ABABAB.....is called hexagonal close packed structure. In ccp there are three layers, the third layer we can call it as C, located at the interstices (the gaps between the atoms) of A and B, so that the stacking sequence will be ABCABCABC.....[3]. In almost all the calculations for simplicity we are considering atoms as hard spheres and assume that these spheres close to each other. Atomic packing factor determines the ratio between the volume occupied by the atoms to the volume of the cell and coordination number is the number of nearest neighbors. For a sc the coordination number is six, eight for bcc and 12 for fcc in unit cells. Lattice point, representing common meeting point for unit cells, for a sc the number of lattice point associated with the unit cell will be one, two for bcc and four for fcc.[4].

There is a nomenclature system for indexing the distance between atoms in a crystals and angles between the interatomic bonds in the unit cell connecting those atoms. Based on the intercepts with the crystallographic reference axes Miller introduced a system to label the crystal planes hence called Miller indices. Figure 1 shows the illustration of determining the Miller indices of a plane.[5]
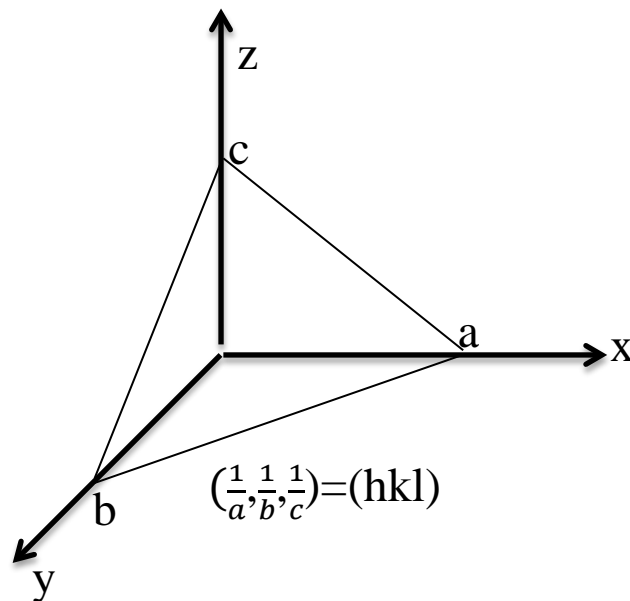
Figure 1: *Determining crystallographic indices for a plane using intercepts with axes.*

Through the following procedure we can determine the Miller indices of any plane in an arbitrary crystal system.

(i) First we need to define the x, y, z axes and take the intercepts on the axes in terms of lattice constants a, b, c

(ii) By taking the reciprocal of those intercepts and reduce them into three integers in a closed parentheses (hkl) which represents a single plane or a set of parallel planes called Miller indices of the plane, where h, k, l are integers.

From the diffraction experiments we can relate the spacing between the successive crystal lattice planes and the diffraction angle to the electron wavelength. From the three direct lattice vectors we can also form a reciprocal lattice vectors $a*, b*, c*$. So we can map the reciprocal lattice of a crystal from the corresponding diffraction pattern of the particular crystal. We can also distinguish the reciprocal basis vectors from direct basis vectors such that:

$$g = ha* + kb* + lc* \dots\dots\dots\dots\dots\dots\dots\dots\dots\dots\dots\dots\dots\dots\dots\dots\dots (3)$$

The connection between the Miller indices (hkl) and the reciprocal lattice vector g with components (h, k, l) is that, both are perpendicular to each other. For example vector $a*$ the reciprocal vector must be perpendicular to both the direct vectors b and c. These conditions leads to following expressions for reciprocal lattice vectors are;

$$a* = \frac{b \times c}{a.(b \times c)}$$

$$b* = \frac{c \times a}{a.(b \times c)} \quad \left. \right\} \dots\dots\dots\dots\dots\dots\dots\dots\dots\dots\dots\dots\dots\dots\dots\dots\dots (4)$$

$$c* = \frac{a \times b}{a.(b \times c)}$$

Due to the connection between direct and reciprocal lattice vectors we can often denoted the reciprocal lattice vector g with Miller indices as subscripts is g_{hkl}. Also the perpendicular distance intersecting the direct basis vectors from the origin is called interplanar spacing d_{hkl}, so that the length of a reciprocal lattice vector is equal to the

13

inverse of the spacing between the consecutive lattice planes in a crystal. Therefore the relation between g_{hkl} and d_{hkl} is;

$$g_{hkl} = \frac{1}{d_{hkl}} \ldots\ldots\ldots\ldots\ldots\ldots\ldots\ldots\ldots\ldots\ldots\ldots\ldots\ldots\ldots\ldots\ldots\ldots..(5)$$

Since different crystal systems have difference in interplanar spacing because lattice parameters are different in each other. For example, cubic crystal system have restrictions on conventional cell axes $a = b = c$ and angles between them $\alpha = \beta = \gamma = 90^0$, therefore the interplanar spacing is;

$$d_{hkl} = \frac{a}{\sqrt{h^2+k^2+l^2}} \ldots\ldots\ldots\ldots\ldots\ldots\ldots\ldots\ldots\ldots\ldots\ldots\ldots\ldots\ldots\ldots\ldots(6)$$

And for hexagonal system:

$$d_{hkl} = \frac{1}{\left[\frac{4(h^2+k^2+hk)}{3a^2}+\frac{l^2}{c^2}\right]} \ldots\ldots\ldots\ldots\ldots\ldots\ldots\ldots\ldots\ldots\ldots\ldots\ldots..(7)$$

Another important thing while dealing with the hexagonal system it is common to use four index Miller-Bravais indices for representing directions and planes. Instead of the three basis vectors there is an extra basis vector which is a combination of the other two vectors which comes 120^0 to both the x and y axis, like for example all the faces of a pencil all are parallel to the z axis. For example $[uvtw]$ represents direction and $(hkil)$ for plane. Where $i = -(h + k)$ which is proportional to the reciprocal intercept of the plane with one of the basis vector. We can relate the extra index to the three index as $[u'v'w']$. Therefore the vector t is;

$t = u'a_1+v'a_2+w'c = ua_1+va_2+ta_3+wc$, where a_1, a_2, a_3 and c are the four basis vectors representing the four index system.[6] The correct transformation relation from 4-index Miller-Bravais to 3-index Miller for hexagonal system is;

$u' = u - t = 2u + v$

$v' = v - t = 2v + u$ $\quad \ldots\ldots\ldots\ldots\ldots\ldots\ldots\ldots\ldots\ldots\ldots\ldots\ldots.(8)$

$w' = w$

The above mentioned conditions should be satisfied for the formation of a good crystal structure under different crystal systems for example cubic, hexagonal etc. For making semiconductor devices cubic and hexagonal systems are most common. Commonly occurring crystal structures in nature are diamond (example silicon, germanium), sodium chloride (NaCl) structure, zinc blende (ZB), wurtzite (WZ) etc During the TEM characterization study commonly observed crystal structures are ZB and WZ, so more emphasis will be given explaining these two. The crystal structure including the stacking sequence of ZB and WZ are shown in figure 2 (a) and (b). ZB also known as sphalerite is coming under ccp, the lattice type is fcc and two atoms in the basis are different. Bulk compound semiconductors such as GaAs, CdS, AlAs etc which are used for optoelectronic devices are coming under this group. The positions of atoms are one at $(0,0,0)$ and the other at $\left(\frac{1}{4}, \frac{1}{4}, \frac{1}{4}\right)$. In the case of WZ the lattice is hexagonal and the nearest neighboring bonds are tetrahedral. The difference in the stacking sequence is ABCABC ....for ZB and ABAB ....for WZ

Zinc blende (ZB)   **Wurtzite (WZ)**
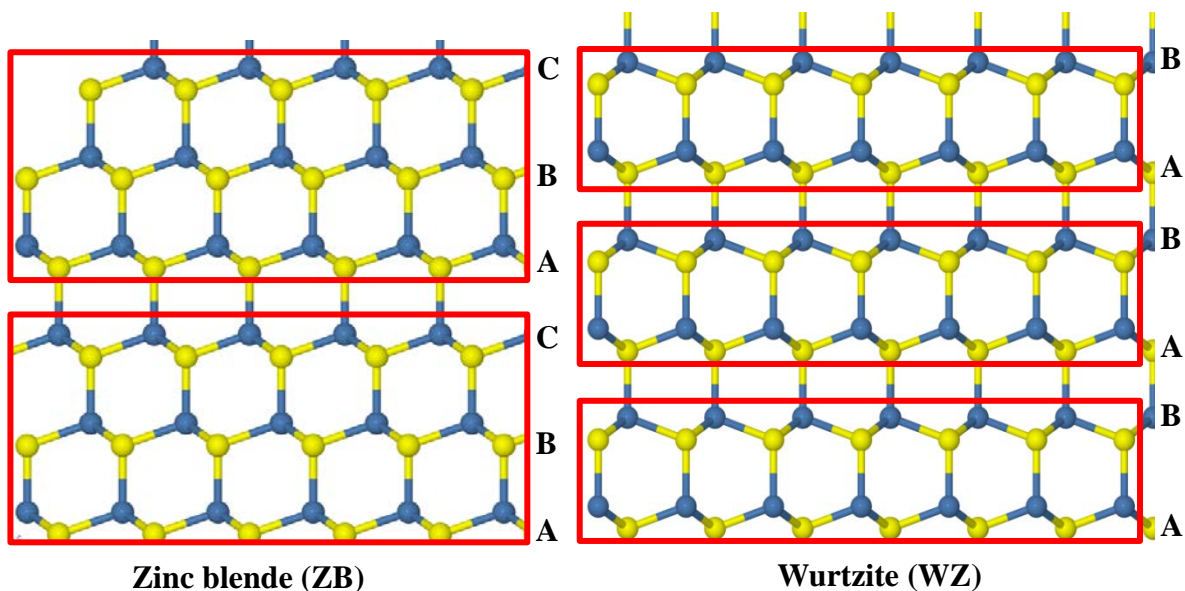
Figure2 (a) & (b): Atomic model illustrating ABCABC...packing for ZB and ABAB... packing for WZ crystals structures. (Made in Jmol software)

2.2 Crystal defects

A perfect crystal is a crystal with no impurities or defects, but most of the high performances devices are based on crystalline semiconductor materials are far from perfect crystals. Common defects in semiconductor materials are point defects, line defects or dislocations, planar and volume defects and twinning. A point defect is very confined, which affects the periodicity of the crystals unit cells. For example in the case of GaAs , one of the atoms say Ga, instead of sitting in the Ga sub lattice it sites in the As sub lattice or vice versa is a kind of point defect called anti-site defect. Also an atom is sitting in between the lattice points called interstitial is considered as a kind of point defect. In comparison with point defects line defects or dislocations involve a very large number of atomic sites which can be connected by a line. Crystal bonds are broken due to the slip in the crystal and are reconnected with the atoms after the slip is a kind of dislocation defect. These kinds of defect can commonly occurred during the growth of lattice mismatched heterostructures.[7]

Planar and volume defects such as stacking faults, twinning etc. can commonly see in polycrystalline materials. In twinning parts of the crystal are oriented with respect to another according to certain symmetry rules. The most commonly occurred twinning is that one part of the crystal structure is the mirror image of other part in a particular crystallographic plane called twinning plane and the other type is the rotation twin. Rotation twin maintains the polarity of the crystal and the bond over the twin is heteroatomic whereas in mirror twin reverses the crystal polarity and the bond over the twin is homoatomic[8].

Twins are the common structural defects in ZB materials especially in III-V NWs. There are two twin types often denoted as ortho and para twins with different symmetry operation. In ortho twin the crystal structure is rotated 60^0 normal to the twin plane in the <111> growth axis, so that the stacking sequence changes from ABCABC to CBACBA. In para twin the crystal structure is rotated 180^0 normal to the twin plane and the stacking sequence will be completely mirrored from ABC… to ACB… stacking. The plane of contact between two parts which coincides the twinning plane is called composition plane[9], which is the crystallographic plane that separates the two twins. The difference between a

twin plane and stacking fault is that, in stacking fault there is a local disturbance in the stacking sequence and this continues in the same manner after every stacking faults. Twinning in crystals can happen due to different causes, for example during crystal growth, phase transformation from one crystal structure to another within a material etc which depends on the growth conditions. Deformation by twinning in a crystal reproduces the crystal structure in a new orientation. For example in the case of ccp crystals, one part of the crystal is the mirror image of the other part in a {111} plane, because the composition plane is also in a {111} plane. This changes the stacking sequence ABCABCABC... to ABCABCBACBAC... and this change in the stacking creates a thin layer of hcp that is BCB a sequence in the WZ structure associated with its characteristic energy. In the case of ZB fcc crystal structure the twinning's are closely related to the the twins in ccp crystals, the structures of twin are related by a rotation of 180^0 about the normal to the corresponding plane. Macroscopically we can explain the twinning due to growth is that twin orientations with respect to the original crystal are lamellae that have experienced a homogeneous shear so that twin lamella is obtained at the interface between the twin plane and the composition plane[9]. During this twin orientation, lattice reorientation and atom movements are occurs at the twinning plane. Very surprisingly a structural modification in the ZB phase was seen during the NW characterization that is periodic twinning. The twin planes that have constant spacing within a crystal form a Twinning Super Lattice (TSL) [10].

2.3 General Theory of Diffraction from Crystals.

This section gives a detailed discussion about how the diffracted waves emitted from different atomic arrangements in crystals. The theory of diffraction is based on Fultz and Howe [11]. Diffraction is a collective phenomenon based on the phase relationship between the waves that going out from individual atoms in crystals and the result is a set of spots or rings which is certainly an evidence of the wave behavior. The wavelet from individual atoms from crystals scattered coherently and allows constructive interference which comprises the diffraction pattern. Therefore the diffraction pattern shows the spectrum of real periodicities and spatial arrangement of atoms in a material. Bragg's law explained that the wavelength (λ) of the incident waves in crystals are comparable to the atomic spacing (d) in crystals and is expressed mathematically as;

17

$2d\sin\theta = n\lambda$.. (9)

The general theory of diffraction pattern describes the wave interference phenomenon due to the scattering of waves from the center of individual atoms from the crystal. The derivation that explained here in this section is applied for any wave diffraction by a group of atoms. The waves that incident on each atoms which interacts with the electron cloud of the atom, must have wavelengths comparable to the spacing between the atoms and each atom contributes diffracted scattered x-ray waves which is proportional to its atomic scattering factor f. Figure 3 shows the vector representation of the wave scattering in materials.
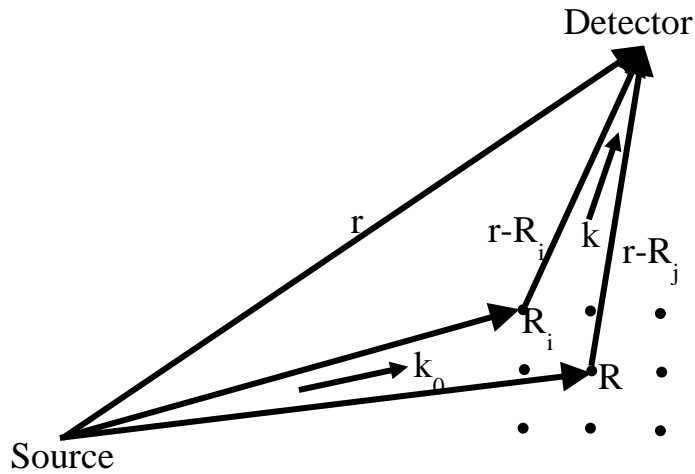
Figure 3: *Electron scattering from a group of atoms in crystals between the scattered and incident wave.*

In figure 3, R_i and R_j are the two different positions of atoms in the material. From the source there is an incident plane wave ψ_0 which describes the structure of the wave, hits the atom R_i at time t' and we get coherent elastic scattering from R_i. Like this we get coherently scattered wavelets from different atoms in the material and the detector detects the diffracted waves from all atoms which we can call it as diffraction. We can explain the process of wave diffraction from a material mathematically. When a plane wave ψ_0 is incident at an atom at R_i at time t' is;

$$\psi_0(R_i, t') = Ae^{i(k_0.R_i - \omega t')}$$... (10)

Where k_0 is the incident wave vector.

For electron the incident plane wave ψ_0 interacts with the nucleus and electron cloud of the atom creates an outgoing wave. Where ψ_i is the coherently scattered outgoing wave at the detector which is proportional to the amplitude A of the incident wave times the atomic scattering factor (R_i). The atomic scattering factor $f(R_i)$ which depends on the difference in the incident (k_0) and the outgoing (k) wave vectors and is very particular to the type of atom at R_i.

$$\psi_0(r, R_i, t) = f(R_i)\psi_0(R_i, t')e^{i[k.(r-R_i)-\omega(t-t')]} \dots\dots\dots\dots\dots\dots (11)$$

Where $t - t'$ is the phase of the wave when it travels from R_i to the detector during the time t'

Substitute (10) for $\psi_0(R_i, t')$ in equation (11) and solve we get

$$\psi_0(r, R_i) = f(R_i)Ae^{i[-(k-k_0.R_i + k.r - \omega t)]} \dots\dots\dots\dots\dots\dots\dots (12)$$

Or we can rewrite the above equation for coherently scattered wave for one atom in the material of the form

$$\psi_0(r, R_i) = f(R_i)Ae^{i(-\Delta k.R_i + k.r)} \dots\dots\dots\dots\dots\dots\dots\dots\dots (13)$$

Where $\Delta k = k - k_0$ is the scattering vector which is controlled by the angle to the detector and also ignores the time t and frequency ω of the waves, since we are working with spatial co-ordinates. Therefore the total diffracted wave from a material at the detector is the sum of coherently scattered wavelet from all N atoms in the material.

$$\psi_i(r') = A\sum_{J=1}^{N} f(R_i)Ae^{i(-\Delta k.R_i + k.r)} \dots\dots\dots\dots\dots\dots\dots\dots.(14)$$

In reality we can neglect the intensity term A and phase factors involving r because we never know the positions of the source and detector. Therefore we can write equation (14) as a function of Δk the scattering wave vector because we cannot adjust the position of the atoms. Equation (14) becomes;

$$\psi_i(\Delta k) = \sum_{j=1}^{N} f(R_i)Ae^{-i\Delta k.R_i} \dots\dots\dots\dots\dots\dots\dots\dots\dots (15)$$

Equation (15) shows that the diffracted wave is proportional to the Fourier transform of the scattering factor distribution in the material. Finally equation (15) consists only Δk which is normal to the diffracting planes, because of the elastic scattering wave vectors k and k_0 have same length, so the length difference in wave vectors $k - k_0$ is not interesting. Figure 4 shows the vector representation of relationship between Δk and θ for elastic scattering which we can see that the direction of Δk is the normal of the diffracting planes k_0 and k

Where $\Delta k = k - k_0 = 2k\sin\theta$
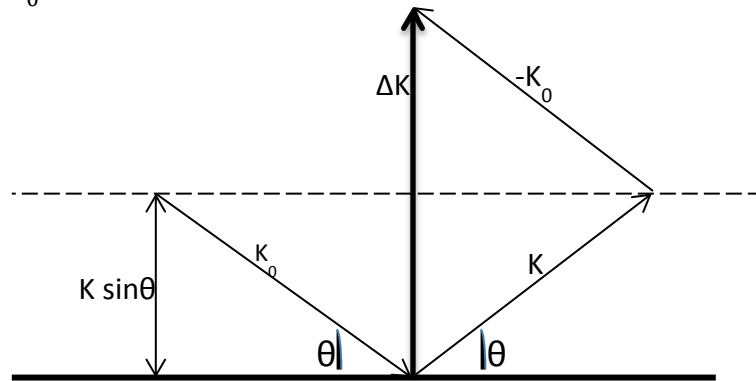
Figure 4: *The vector relationship between ΔK and θ for elastic scattering showing that the direction of Δk is the normal of the diffracting planes k_0 and k.*

We can consider diffraction from a simple lattice, having only one type of atom per unit cell of the lattice, so that we can substitute our primitive lattice vectors which are same as the position of all atoms in equation (15). Therefore equation (15) becomes;

$$\sum e^{-i\Delta k.R_i} = \sum e^{-i\Delta k(ua+vb+wc)} \dots\dots\dots\dots\dots\dots\dots\dots\dots\dots\dots\dots\dots\dots \ (16)$$

For to get a maximum wave amplitude when;

$$\Delta k(ua + vb + wc) = 2\pi.integer \dots\dots\dots\dots\dots\dots\dots\dots\dots\dots\dots\dots \ (17)$$

For all possible combinations of $\{m, n, o\}$, because $e^{2\pi.integer} = 1$

There are another three vectors which is analogous to our primitive lattice vectors denoted by $\Delta k' = ha*+kb*+lc*$ which also satisfies $\Delta k'(a, b, c) = 2\pi.integer$, leading to a strong diffraction. This means that diffraction occurs when Δk is a vector of the reciprocal lattice,

so that $\boldsymbol{\Delta k} = \boldsymbol{g}$. This is the Laue condition for diffraction. Where g is the arbitrary reciprocal lattice.

2.4 Ewald Sphere and Bragg's law.

The Ewald sphere construction is a geometrical implementation of the Laue condition for diffraction $\boldsymbol{\Delta k} = \boldsymbol{g}$ by Ewald. Figure 5(a) shows the geometrical representation of Ewald sphere. The Ewald sphere describes the incident wave vector k_0 and all possible diffracted wave vectors k. The wavevector k_0 is pointed towards the reciprocal lattice which acts as the origin and the tips of all possible k vectors lie on the Ewald sphere. Therefore the geometrical formation of Laue condition says that, diffraction g occurs when the Ewald sphere touches a point on the reciprocal lattice point. Figure 5(b) shows that Ewald sphere is equivalent to Bragg's law.
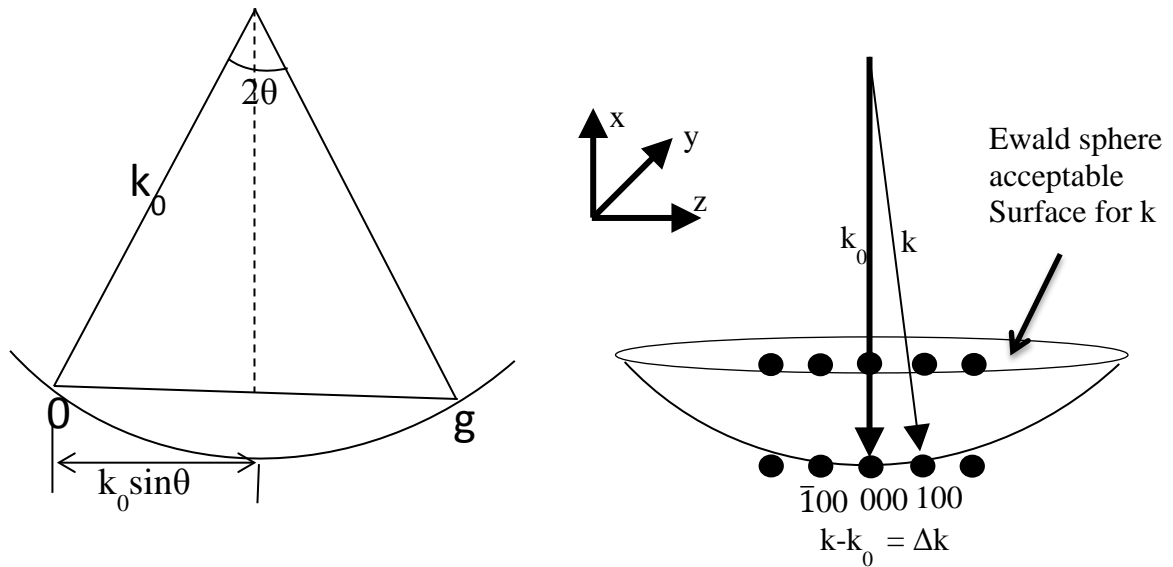
Figure 5: *(a) Ewald sphere construction diffraction occurs when the ewald sphere touches a point on the reciprocal lattice and the criterion is satisfied for (100) and $\bar{1}00$ diffraction (b) Geometrical representation of Ewald sphere construction is a graphical implementation of Laue condition, so that it is equivalent to Bragg's law.*

From figure 5(a)

$$sin\theta = \frac{g/_2}{k}\text{..} (18)$$

From the definition of wave vector and reciprocal lattice vector:

$$g = \frac{1}{d} \text{ and } k = \frac{1}{\lambda}.$$ ……………………………………………………………..(19)

Substitute equation (19) in equation (18) we get the Braggs law:

$$2d \sin \theta = \lambda$$ ……………………………………………………………… (20)

While working with TEM we need to keep in mind the rules for working with the Ewald sphere. They are;

(1) The Ewald sphere and the reciprocal lattice points are attached at the origin of the reciprocal lattice, therefore tilt either the reciprocal lattice or Ewald sphere are operate about this fixed pivot point.

(2) Tilting the sample is achieved by tilting the reciprocal lattice at same angle in same direction, because the reciprocal lattice is attached to the crystal.

(3) Tilting the direction of the incident beam is achieved by tilting the Ewald sphere by same quantity, because the Ewald sphere surrounds the incident beam and is attached to it. When we tilt the specimen the viewing screen and the Ewald sphere is fixed, but the various points on the reciprocal lattice of the specimen move into the viewing screen. This means that the diffraction g occurs when the Ewald sphere touches the reciprocal lattice point, that is $\Delta k \sim g$

Alternatively when we tilt the incident beam, we are rotating the transmitted beam on the Ewald sphere. By tilting this illumination and diffraction we can do axial dark-field imaging. If we tilt the direction of the incident electrons away from the optic axis by an angle, the diffracted rays travels straight down the optic axis, we get dark field images with best resolution.

2.5 Structure Factor rules for diffracted waves from crystal.

The structure factor is a mathematical function which describes the phase and amplitude of a diffracted wave from the lattice planes of a crystal which is denoted by F_{hkl} and it is the amplitude scattered by the atoms in the unit cell by the amplitude scattered by a single electron. We can directly relate the intensity of the diffracted beam to the amplitude of the structure factor. From the structure factor determination we can deduce the positions and anisotropic displacements of the scattering atoms from a crystal. Every atom in the unit cell contributes to every F_{hkl} according to the chemical nature of the material and position in the unit cell. The general expression for the structure factor is;

$$F_{hkl} = \sum f e^{2\pi(hx+ky+lz)} \dots\dots\dots\dots\dots\dots\dots\dots\dots\dots\dots\dots\dots\dots\dots\dots\dots\dots \quad (21)$$

This equation is applicable for all the atoms in the unit cell and all the crystal lattices. If we insert the atomic coordinate values into the equations for F_{hkl} to calculate the structure factor for the corresponding crystal structures. If there is more than one atom in the basis of the unit cell the structure factor determination is more interesting, because waves which are scattered by the atoms in the basis leads to the precise cancellation of some diffractions which does not allows certain combinations of h, k, l in the diffraction pattern. So a structure factor consists of two values which depends whether the sum of $h + k + l$ is even or odd. The structure factor formula and rules for fcc, bcc and hcp are shown in the table (2) below.[12]

Table 2: The structure factor formula and rules for fcc, bcc and hcp.

fcc	h, k, l all even or all odd	$F = f\{1 + e^{\pi i(h+k)} + e^{\pi i(h+l)} + e^{\pi i(k+l)}\}$
bcc	h, k, l must be even	$F = f\{1 + e^{\pi i(h+k+l)}\}$
hcp	$h + 2k = 3m$, even, multiple of 3 $h + 2k = 3m \pm 1$, even or odd	$F = f\left\{1 + e^{2\pi i(\frac{h}{3}+\frac{2k}{3}+\frac{l}{2})}\right\}$

This means that the structure factor rules determine the properties of the lattice and it does not depends the atomic arrangements within the volume of the unit cell.

The structure factor calculation for ZB GaAs and WZ GaAs is following. The position of four Ga and four As atoms in the basis of ZB GaAs are at;

Ga: $(0,0,0), \left(\frac{1}{2},\frac{1}{2},0\right), \left(\frac{1}{2},0,\frac{1}{2}\right), \left(0,\frac{1}{2},\frac{1}{2}\right)$

As: $\left(\frac{1}{4},\frac{1}{4},\frac{1}{4}\right), \left(\frac{3}{4},\frac{3}{4},\frac{1}{4}\right), \left(\frac{3}{4},\frac{1}{4},\frac{3}{4}\right), \left(\frac{1}{4},\frac{3}{4},\frac{3}{4}\right)$

Substitute the Ga and As coordinates of atoms in equation for fcc from table (2) gives;

$$F_{ZB} = \left\{ f_{Ga} + f_{As} e^{\frac{\pi}{2}i(h+k+l)} \right\} F_{fcc} \dots\dots\dots\dots\dots\dots\dots\dots\dots\dots\dots\dots\dots \text{(22)}$$

Therefore the structure factor rules for ZB GaAs are;

$F = 0,$ if h, k, l are mixed.

$F = 4(f_{Ga} \pm i f_{As}),$ if h,k,l are all odd.

$F = 4(f_{Ga} - i f_{As}),$ if h, k, l are all even and $h + k + l = 2N$ where N is odd.

$F = 4(f_{Ga} + i f_{As}),$ if h,k,l are all even and h+k+l=2N where N is even.

Where N is an integer. The kinematically allowed reflections for ZB GaAs are $(000), (111), (002), (113).$ [13]

The WZ structure of GaAs is to hcp and the position of two Ga and two As atoms in the basis of WZ GaAs are at;

Ga: $\left(\frac{1}{3},\frac{2}{3},0\right), \left(\frac{2}{3},\frac{1}{3},\frac{1}{2}\right)$;

As: $\left(\frac{1}{3},\frac{2}{3},\frac{3}{8}\right), \left(\frac{2}{3},\frac{1}{3},\frac{3}{8}\right).$

Substitute these values of Ga and As coordinate atoms in structure factor equation for hcp gives;

$$F_{WZ} = f_{Ga}\left\{e^{-2\pi i\left(\frac{1}{3}h+\frac{2}{3}k\right)} + e^{-2\pi i\left(\frac{2}{3}h+\frac{1}{3}k+\frac{1}{2}l\right)}\right\} + f_{As}\left\{e^{-2\pi i\left(\frac{1}{3}h+\frac{2}{3}k+\frac{3}{8}l\right)} + e^{-2\pi i\left(\frac{2}{3}h+\frac{1}{3}k+\frac{3}{8}l\right)}\right\}..(23)$$

$$F_{WZ} = \left\{f + f_{As}e^{-\frac{3}{4}i\pi l}\right\}F_{hcp}\dots\dots\dots\dots\dots\dots\dots\dots\dots\dots\dots\dots\dots\dots\dots\dots\dots (24)$$

For the analysis for writing the structure factor rules for WZ structure we take the square of the amplitude of F_{hcp} then;

$$F^2 = 0, \qquad\qquad\qquad\qquad \text{if } h + 2k = 3m \text{ and } l \text{ is odd.}$$

$$F^2 = 4f^2 = 4(f_{Ga}^2 + f_{As}^2), \quad \text{if } h + 2k = 3m \text{ and } l \text{ is even.}$$

$$F^2 = 3f^2 = 3(f_{Ga}^2 + f_{As}^2), \quad \text{if } h + 2k = 3m \pm 1 \text{ and } l \text{ is odd.}$$

$$F^2 = f^2 = (f_{Ga}^2 + f_{As}^2), \qquad \text{if } h + 2k = 3m \pm 1 \text{ and } l \text{ is even.}$$

Where m is an integer and the kinematically allowed reflections for WZ GaAs are $(1\bar{1}0), (002), (1\bar{1}1).$[13]

2.6 Zone axis patterns

While doing the diffraction experiments it is better to make zone axis pattern before insert the selected area aperture for the diffraction pattern from the sample region that we selected. We also need to make sure that our sample is in eucentric position which means that the sample region illuminated by the beam should not move laterally when we tilt the sample. Then tilt the specimen around both or one of the tilt axis in the goniometer until we observe many diffracted beams on the screen. We can adjust the specimen tilts so that we can obtain a symmetric pattern obtained by "closing the circle" called Laue circle with respect to the center of the screen. When the crystal is oriented such that a zone axis is parallel to the incident beam and also the planes that belonging to that zone will all be closer to the Bragg orientation and their reciprocal lattice vectors are all lie in a plane which is tangent to the Ewald sphere. Such symmetric two dimensional array of spot pattern is known as zone axis diffraction pattern. Then insert the SAD aperture and we can see our diffraction pattern from the area of sample that we selected.

2.7 Kikuchi lines

When the sample is thick and transparent to electrons, incoherent scattering provides a diffuse background for the diffraction pattern. On the top of this diffuse background intersecting sets of bright or dark straight and regularly arranged lines formed. These sets of lines are called Kikuchi lines which gives the crystallographic information about the sample. Kikuchi lines are originate due to the multiple scattering from crystals, an incoherent followed by a coherent Bragg diffraction. We can explain the formation of Kikuchi lines theoretically with the help of two beams coming out from the crystal. One beam consists of electrons that were Bragg diffracted with electrons that scattered incoherently by an angle θ and they were not diffracted by crystal planes. The second beam which consists of forward scattered electrons that were Bragg diffracted into the forward direction. Due to this stronger incoherent scattering in the forward direction, so there is more loss of electrons by secondary Bragg diffraction from the second beam than from first beam. These electron lost from the forward beam by secondary Bragg diffraction are added to the first beam and also some of the electrons are transferred from first beam to the second beam, so that the net electron intensity in the diffuse background is therefore transferred from the second beam and added to the first beam. Therefore in the pattern the diffuse background has a variation in the intensity of two beams, one dark and one bright separated by an angle 2θ. This intensity variation in occur in the diffuse background can occur in any direction that makes Bragg angle to a crystal plane. In 3D these set of rays form pairs of cones which are called Kossel cones. If there is diffuse background intensity in the diffraction pattern is very high, Kikuchi lines become more visible.

2.8 Double diffraction

Double diffraction occurs when the specimen is thick and if the specimen is thin enough for TEM only single scattering need to be considered. In double diffraction an electron is diffracted twice before entering the specimen, needs that the beam from first diffraction acts as the incident beam for the second diffraction. This means that there is an occurrence of forbidden diffractions when the specimen is of modest thickness or an incoherent scattering contributes a diffused background for the diffraction pattern. In the figure6

26

showing the diffraction pattern from a thin specimen and how the second diffraction the intensity varies for the forbidden reflection. On the left side the diffraction pattern from a thin crystal and nothing at the forbidden locations. When the crystal becomes thicker the diffracted beams are stronger. In TEM diffraction for small Bragg angles, these diffracted beams are close with the orientation to the incident Bragg angle, so that these diffracted beams acts as the incident beam for making the same type of diffraction pattern and the new diffraction patterns are located at forbidden locations around each strong diffraction spots.
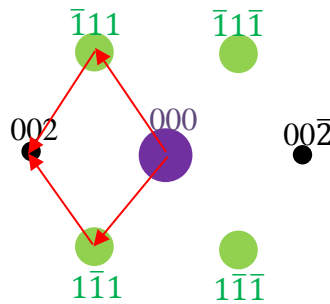

Figure 6 Schematic representation of an example for double diffraction. In figure diffraction pattern of a diamond cubic lattice (one atom per basis), the black spots are systematically absent. The intensity of the black spots becomes visible due to the multiple scattering (shown by red arrow) through $\bar{1}11$ and $1\bar{1}1$ scattering vectors.

Transmission Electron Microscopy.

2.9 Introduction to TEM.

Transmission Electron Microscope (TEM) is a sophisticated electron optical system having the capability of displaying images of a thin specimen with a magnification range about 10^3 to 10^6. In 1925 Louis de Broglie theorized the wave like characteristics of electrons. Later, Davisson and Germer and Thompson and Reid demonstrated the wave nature of electrons through their classic electron diffraction experiments. In 1930s, the experimental work with electron lenses was done by Ernst Ruska in Berlin, which was the most crucial step for the development of TEM and many years later he received the Nobel prize for his contributions in the field and TEMs were developed by several commercial companies.[12] Today, TEMs are powerful tools to image details down to atomic level, to understand the microstructural characterization of materials, to provide the phase, structural, crystallographic data of materials etc. High energy electrons from the source interact with the atoms and electrons in the specimen which helps to visualize the microstructural details. The viewing screen of electron microscope translates electron intensity to light intensity that we record or observe photographically. Resolution or resolving power is the smallest distance between two points that we can resolve with our eyes is about 0.1-0.2 mm. From the Rayleigh criterion for light microscopy the resolution (δ) of TEM is $\delta = \frac{0.61\lambda}{\mu sin\beta}$. Where λ the wavelength of the electron and the value is related to their energy from de Broglie's relation $\lambda \sim \frac{1.22}{\sqrt{E}}$, β the semiangle of collection of the magnifying lens and μ the refractive index of the viewing medium. The major source of contrast in TEM images are elastically scattered electrons and they create the intensity distribution of diffraction patterns can be observed. When a high energy electron beam interacts with the specimen several types of signals can be detected which can provide information about the samples chemical composition, topography, crystallography etc. Figure 7 a schematic representation of sample interaction with high energetic electrons.
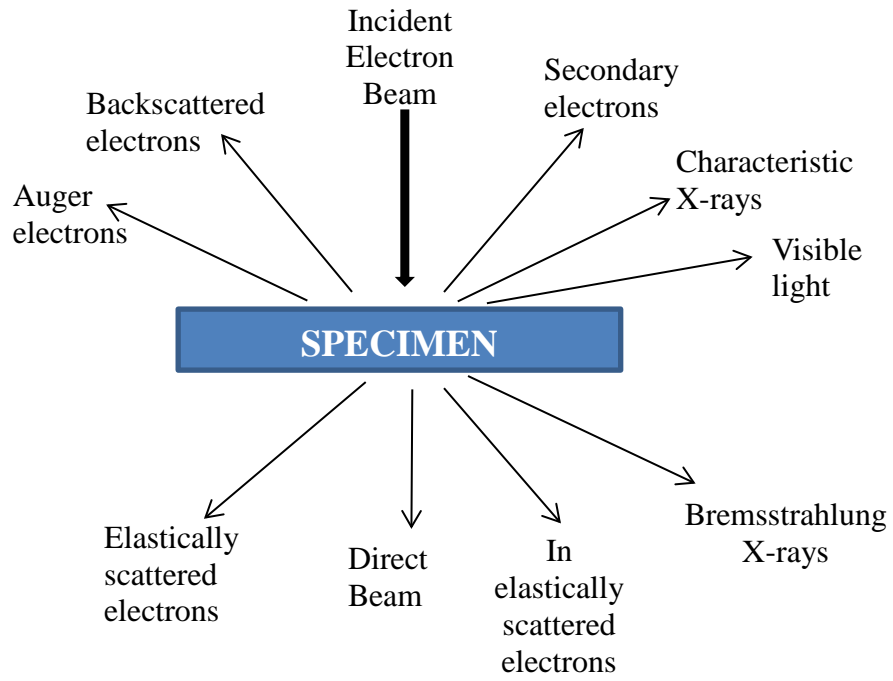
Figure 7: Sample interaction with high energetic electrons.

2.9.1 The conventional TEM and its optics.
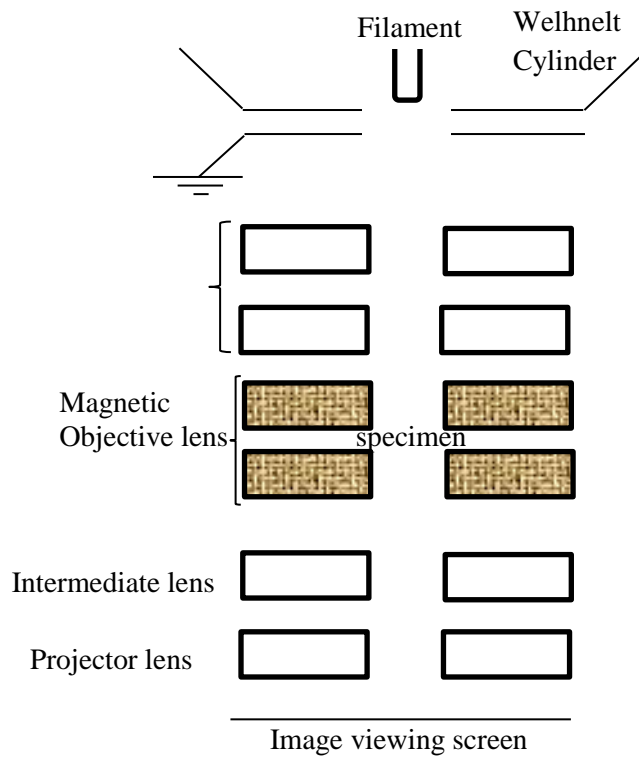
Figure 8: (*a*) *CM30 TEM used for this study.* (*b*) *Block diagram for typical TEM* [23].

We can divide the optical system of TEM into three main components which are,

- Illumination system
- Specimen stage
- Imaging system

The illumination system contains the electron gun, condenser lenses and condenser aperture that focus the electron beam onto the specimen. The design and operation of the illumination system determines the diameter of the electron beam focusing on the specimen and the intensity level in the TEM image.

The specimen stage which contains the specimen that needs to be characterized allows specimen to be moved, held stationary, inserted or withdrawn from TEM. The important factor that determines the spatial resolution of the TEM image is the mechanical stability of the specimen stage.

The imaging system produces a magnified image of the specimen. It contains objective lens, diffraction lens, projection lenses and viewing screen. Operation of the imaging system determines the magnification of the TEM image and the spatial resolution that can be obtained from the microscope.

2.9.2 The electron gun

The electron gun produces a beam of high energy electrons that pass through thin specimens for TEM. The electron gun is controlled by three main variables such as the filament current, the feedback resistance and high tension accelerating voltage. Different types of electron source operating on different physical principles for example Thermionic emission, Schottky emission and field emission .TEM used in the current study is based on thermionic emission which will be discussed in detail below. The schematic representation of thermionic emission is shown below.
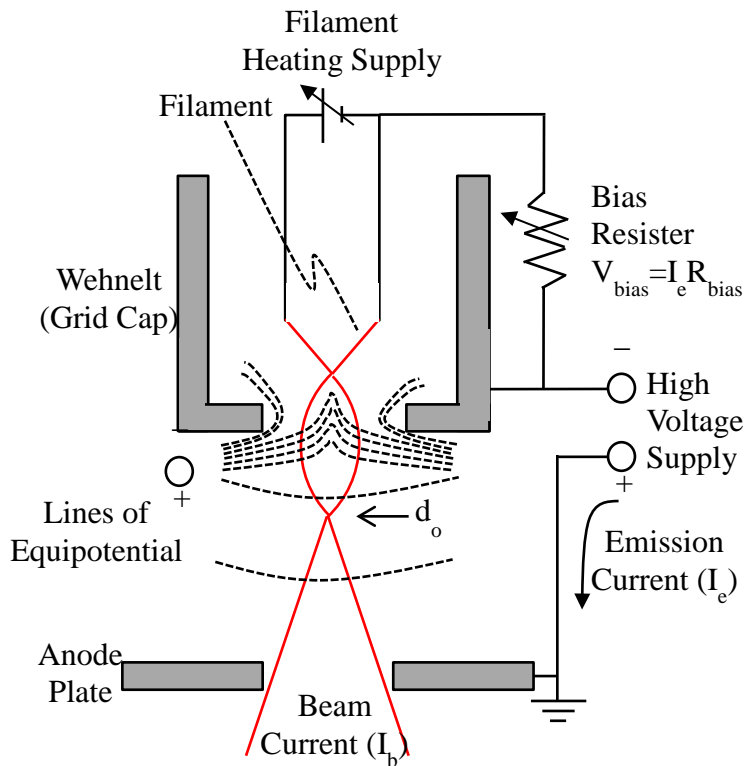
Figure 9: *Schematic representation of thermionic gun[6]. A high voltage is placed between the filament and anode, Wehnelt which acts to focus the electrons into crossover with diameter d$_o$*

The electron gun consists of filament F, Wehnelt electrode W and an anode. The principle behind the thermionic emission is, when the filament is heated to a high enough temperature, some electrons receive sufficient thermal energy to overcome the work function ϕ of the tungsten or vacuum interface and leave the metal. From Richardson's law the physics of thermionic emission which relates the current density J from the source to the temperature T is

$$J = AT^2 e^{-\frac{\phi}{kT}} \dots\dots\dots\dots\dots\dots\dots\dots\dots\dots\dots\dots\dots\dots\dots\dots\dots\dots\dots\dots\dots\dots\dots\dots \text{ (25)}$$

Where A is the Richardsons constant, ϕ the work function and K the Boltzmans constant.

The filament is also called a cathode, which is a V-shaped Tungsten or Lanthanum hexaboride (LaB$_6$) material. The temperature is very high at the tip of the V shaped filament, so most of the emission occurs from the tip. Tungsten has high melting point $3650\ K$, high cohesive energy and low vapour pressure at a temperature of 2500-

3000 K in vacuums. In spite of Tungsten's high work function $\phi = 4.5eV$, $\frac{\phi}{kT}$ can be very low to provide sufficient electron emission [14]. Tungsten can be made into thin wire and can be heated by passing current through it due to its electrical conductivity. Now a days microscopes use LaB_6 material with low work function ($\phi = 2.7$ eV) which does not need to be heated to such a high temperature. LaB_6 is relatively expensive but it lasts longer compared with the tungsten filament.

   Another important component of electron gun is Wehnelt electrode which provides an electrostatic field to the electrons from the filament. Negatively biased Wehnelt electrode restricts the electron emission; it also helps to focus the electrons to a crossover when they accelerate towards the anode which is at ground potential. Wehnelt electrode is designed in such a way that the electron emission is regulated and keeps steady against fluctuations in the filament temperature. It also limit on the maximum usable filament heating current. Wehnelt electrode is self-biased electrically which means that, higher the electron current stronger is the negative bias which further breaks off the electron current. During the alignment of TEM, after few turns of filament knob an image of the filament can be visualized on the viewing screen. When we increase the current again, the image of the filament will get brighter until it reaches saturation level. Due to self-biasing mechanism of the electron gun, further increase the filament current there is no longer effective in increasing brightness. If we heat the filament beyond saturation it increases only the filament temperature but not the brightness, further this reduces the filaments life time[11].
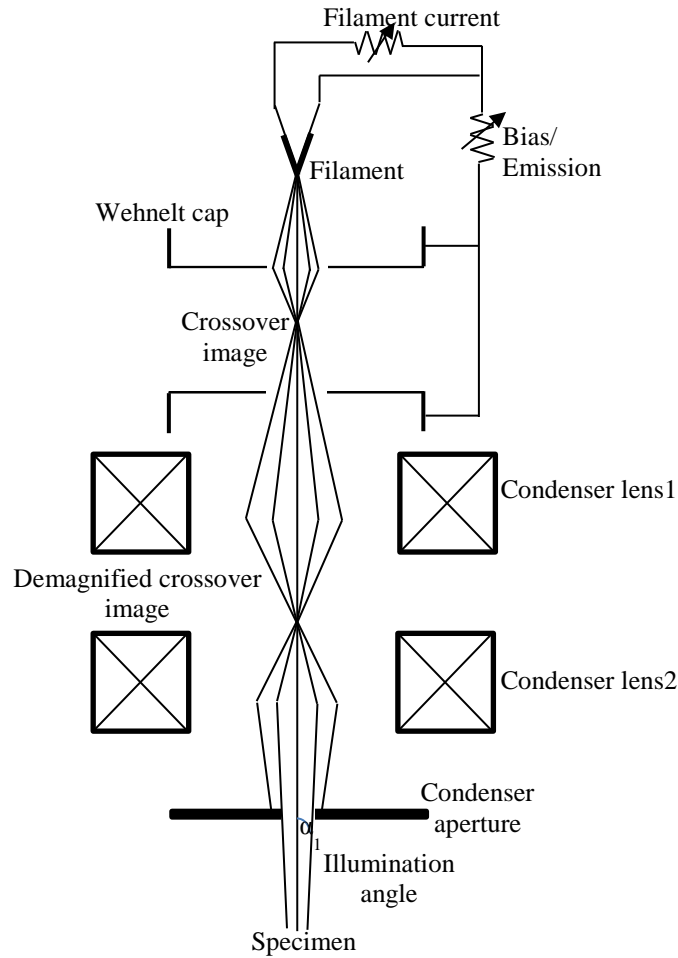
Figure 10: *The illumination system of TEM with thermionic gun and two condenser lenses.*

Figure (10) shows that when electrons pass through the Wehnelt electrode it reaches the anode with high velocity, and then reaches the condenser lenses. The responsibility of the first condenser lens is to demagnify the crossover from the Wehnelt cap and produces a condensed source of illumination in front of the second condenser lens. When the position of the crossover image moves closer to the lens, the demagnification increases with the strength of the first condenser lens. The spotsize knobe in TEM controls the current of the first condenser lens. Changing the strength of the second condenser lens allows the beam to be converged on the specimen, to spread into a set of parallel rays or even into a divergent cone on the specimen. By placing an aperture after the second condenser lens which controls the quality of the beam convergence onto the specimen.

2.9.3 Electromagnetic lenses and apertures.

Focusing of electrons with magnetic lenses and their apertures determines the quality of images and diffraction patterns from TEM. Since the lenses are magnetic, we can change the strength by changing the magnetic field. An idea of electron focusing and various lens operations can be attained through geometrical optics. Figure 11 shows the simple ray diagram to construct an image. There are three rays in this diagram that are (1) ray going to the direction of optic axis (2) ray that goes from the tip of the object through the center of the lens (3) the ray that leaves from the object and travels parallel to the optic axis.
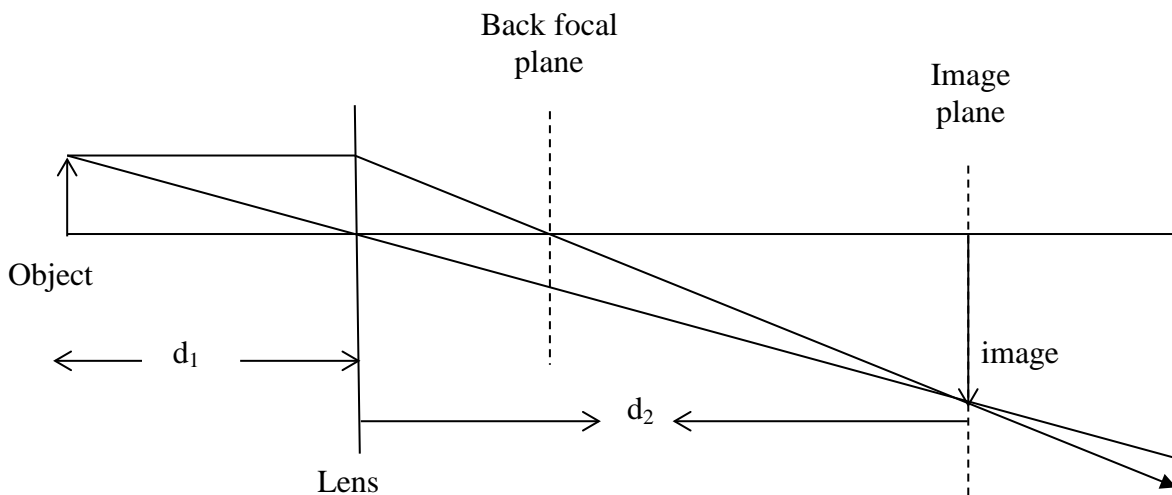
Figure 11: *Simple ray diagram which constructs an image*[11].

Through lens formula we can find the relationship between the distances of the object from the lens d_1, the distance of the image from the lens d_2 and the focal length of the lens f and is given by

$$\frac{1}{f} = \frac{1}{d_1} + \frac{1}{d_2}..(26)$$
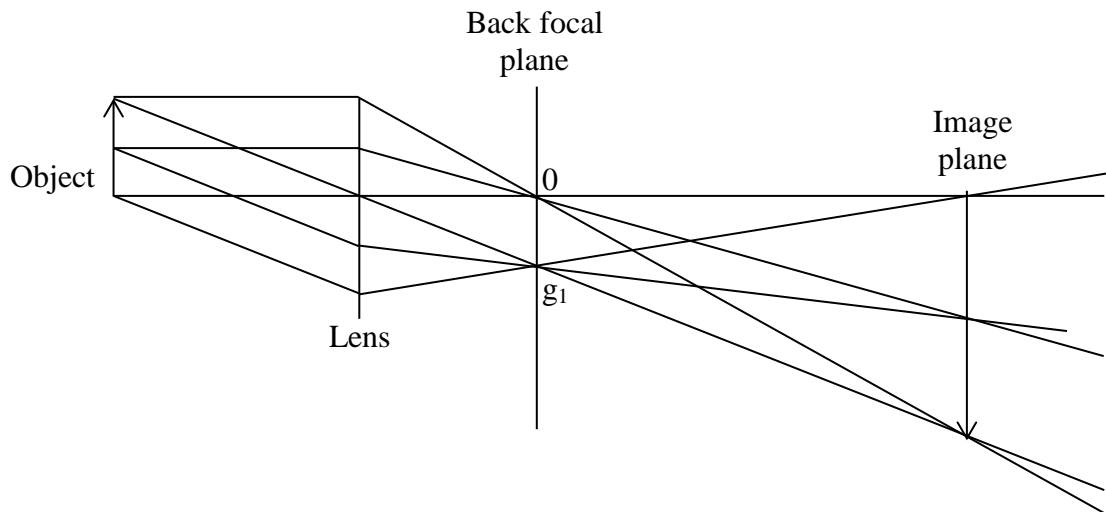
Figure 12: *Detailed ray diagram displaying several rays, rays labeled 0 are parallel when they leave the object and the same for g_1 also, both rays converges in the back focal plane forming an image[11].*

In figure 12 there are several rays and rays which are far away from the optic axis bent more strongly. We can see a back focal plane of the objective lens in figure11 and figure12, which contains grouping of rays that leaves the object or the specimen at the same angle. The diffraction pattern of the specimen is contained in the back focal plane and can be imaged by proper operation of lenses. In TEM, an objective aperture is located at its back focal plane, this aperture is a tiny hole in a plate which is used to select the rays labeled 0 or g_1 while forming an image. When the objective aperture selects the rays that labeled 0 we get a BF image and when rays g_1 is selected by the objective aperture a DF image is formed. The size of the aperture angle of a lens determines the angular range that the lens accepts rays, which is inclined to the optic axis. Aperture angle size determines the resolution of the image from TEM. For example if our lens would be perfect we can use large aperture angle to improve the resolution, so that the Rayleigh criterion for resolution (δ) is satisfied. Blurring by diffraction effects from the edge of the aperture can be minimized with the help of large aperture angle if our lens is perfect. In the case of magnetic lens aperture angle should be small enough to reduce the distortions of off-axis rays from lens aberrations.
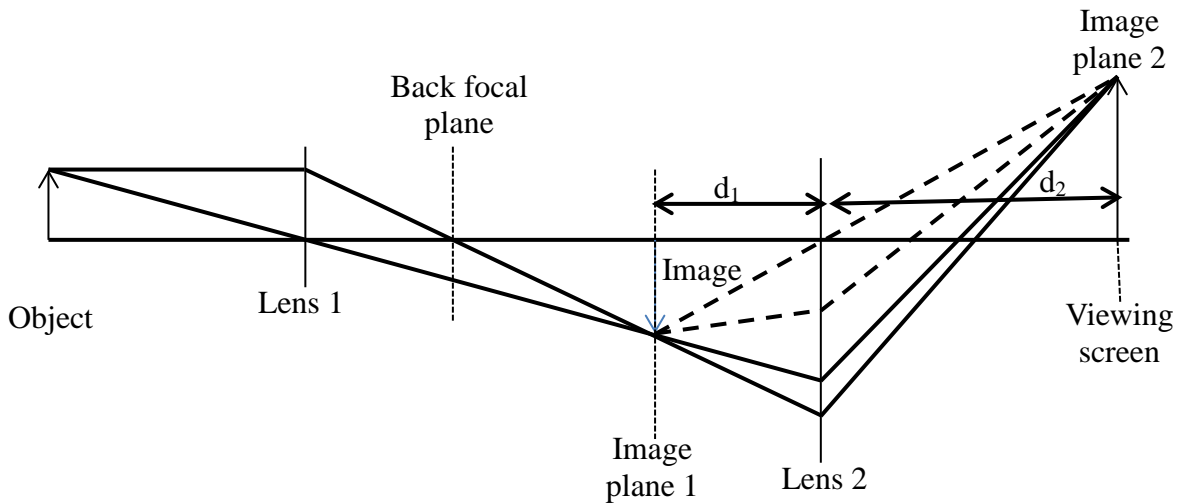
Figure 13: Ray diagram for two lens system for controlling flexible diffraction and imaging.[11]

In TEMs multiple lenses are used for controlling flexible diffraction and imaging. Figure13 shows the ray diagram of two lens system. Lens 1 is the objective lens and lens 2 is the intermediate lens. Different modes of operations in TEM can be changed by increasing the electrical current in the intermediate lens, the lens 2.

In optical microscopes glass lenses are used for image formation, but in TEMs magnetic or electrostatic lenses are applied to deflect electrons. The magnetic lenses are round shaped; its purpose is to focus the electron beam towards the optical axis. In most magnetic lenses there are two pole pieces, made of soft iron with a hole drilled through it. The distance between the two pole pieces is called lens gap and the magnetic field strength is higher near the optical axis between the two pole pieces.

The principle behind the focusing action of magnetic lenses is deduced from the Lorentz force on the moving electron, which is

$$F = -e(v \times B)\ldots\ldots\ldots\ldots\ldots\ldots\ldots\ldots\ldots\ldots\ldots\ldots\ldots\ldots\ldots\ldots\ldots\ldots.(27)$$

This means that the Lorentz force of the electron increases with increasing the magnetic field which is proportional to the focusing strength of the lens.
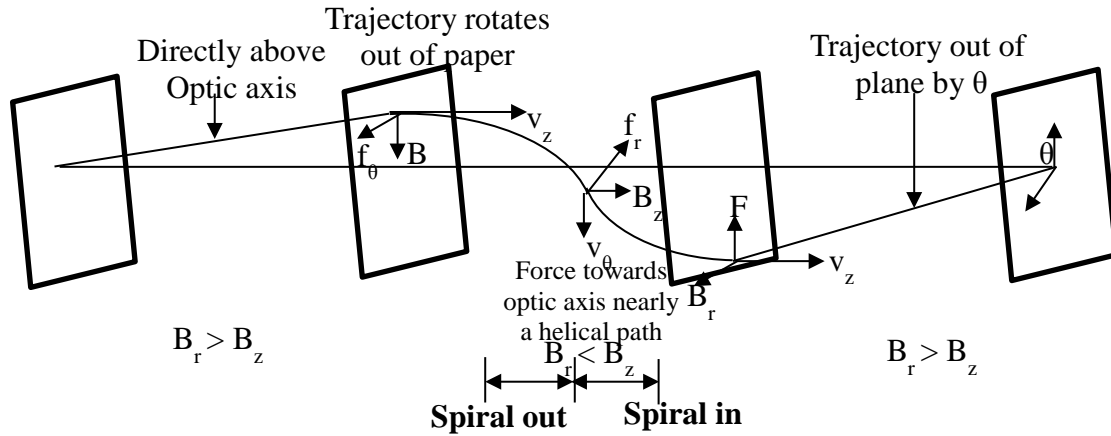
Figure14: *The electron trajectory through a magnetic lens showing the electron that is the image then reaches its final focus after rotations inside the magnetic lens[11].*

Figure 14 shows the electron trajectory through a magnetic lens. The path of an electron that leaves the object plane and focused at the image plane is traced as below. In the beginning, electrons travel at an angle directly above the optic axis and reaches the solenoid. Before it reaches the solenoid where $B_r \gg B_z$, it senses the pre-field. B_r points to the optic axis and B_z points towards right on the left of the lens center. The cross product of velocity v_z and magnetic field B_r gives a force F_θ produces a new velocity v_θ, which rotates the electron trajectory around the optic axis. This spiral movement of electron trajectory rotates with a velocity v_θ and reaches the region where B_z is strong. The cross product of v_θ and B_z gives a new force F_r at the center of the magnetic lens which helps to point the electron trajectory towards the optic axis. Next the electron trajectory travels to the right from the center of the magnetic lens, the velocity v_θ and B_r changes its sign, which is maximum at the center of the magnetic lens. The symmetry of the lens stops the spiraling motion by reducing the velocity v_θ to zero and the electron trajectory moves directly towards the optic axis, focused at the rightmost centre of the image plane. The electron then reaches its final focus after rotations inside the magnetic lens. This means that the image itself is rotated by an angle. The rate of angular rotation increases with the magnetic field strength inside the lens, which increases the current through the lens coil. In latest microscopes this is done automatically but in older microscopes this rotation can be corrected by rotating the images manually.

2.9.4 Lens problems and Resolution

The most important focusing defects in TEMs are lens aberrations, which reduces the spatial resolution of the image. The most common aberrations are the following

- Spherical aberration (C_s)
- Chromatic aberration (C_c)
- Astigmatism

Spherical aberration arises the electron trajectories that are far away from the optic axis, they bent more strongly by magnetic lens field than those rays near the optic axis . This results the formation of a disk rather than a point where all rays meet. The relationship between the diameter d_s of the disk and angle of outer ray through the lens α is:

$$d_s = \frac{1}{2} C_s \alpha^3 \dots\dots\dots\dots\dots\dots\dots\dots\dots\dots\dots\dots\dots\dots\dots\dots\dots \text{(28)}$$

Where C_s is the spherical aberration co-efficient. It is very difficult to make a round magnetic lens with zero spherical aberration. Chromatic aberration arises when electrons with different energies entering a lens will be focused at different locations in the image plane, results disk formation rather than a point where all rays converge. This disk formation is due to the specimen thickness, irregularities of the accelerating voltage and the lens current. Therefore the diameter of the disk d_c can be expressed in terms of convergence angle α and fractional variation of electron beam energy ($\Delta E/E$) is;

$$d_c = C_c \alpha \left(\frac{\Delta E}{E}\right) \dots\dots\dots\dots\dots\dots\dots\dots\dots\dots\dots\dots\dots\dots\dots.. \text{(29)}$$

Where C_c is the chromatic aberration co-efficient.

This can be minimized by making thin specimens so that we can reduce the inelastic scattering of high energy electrons.

Astigmatism arises due to the imperfection in cylindrical symmetry of lens. The electrons diverging from the point object will produce two separate lines of foci, blurs the image and degrades the resolution. By alternatively adjusting the stigmator and focus control knob in TEM corrects the astigmatism and makes negligible effect on image resolution.

Even if there is no lens aberration a single point source cannot be imaged as a point, but imaged as a disk instead of diffraction points called Airy disk. Therefore the classic Rayleigh criterion for resolution is given by

$$d_d = 0.61 \frac{\lambda}{\alpha}$$ ………………………………………………………………………. (30)

Where λ the wave length of the electron, α is the aperture angle of the objective lens and d_d is diameter of the disk. Gun brightness β , is defined as the current density j_0 per semi angle of beam convergence α_p, is also a factor which determines the resolution of the image. TEM experiments need a small beam diameter d_0 on the sample which is determined by the quality of the lens and the performance of the electron gun. The relationship between d_0 , β, α_p, I_p (the total beam current) is given by,

$$d_0 = \frac{\frac{\sqrt{4I_p}}{\beta}}{\pi \alpha_p} = \frac{C_0}{\alpha_p}$$ …………………………………………………………… (31)

so a small beam diameter d_0 can be obtained by either increasing the brightness β or by increasing the semi angle of beam convergence α_p

Resolving power of a microscope is the minimum resolvable distance in the object that can be resolved and easily distinguishable in an image. By summing up the equations of d_s, d_c, d_d, and d_0 we get a general expression for beam size d_p and image resolution. Now C_s -correcters are developed commercially to reduce the spherical aberration and perhaps this situation in microscopes could be changed in future, will have built-in C_s-correctors as standard component.

2.9.5 Modes of operations in TEM

TEMs are the most powerful tools for microstructural characterization of materials. In TEM there are different operations for to characterize materials, some of them are;

- Imaging- Bright Field (BF) , Dark Field (DF) and High Resolution Lattice Imaging.
- Diffraction- Selected Area Diffraction (SAD)
- Bright field and Dark field imaging

Bright field and Dark field imaging

As we discussed earlier in section multiple lenses are used for imaging and diffraction modes in TEM. The main lenses are objective lens and intermediate lens. In simple imaging mode, all the transmitted and diffracted rays from the specimen together form an image at the viewing screen, but poor contrast. Rays from all parts of the specimen meets the back focal plane of the objective lens. But we don't need all the rays in the back focal plane for to form an image, only those rays passing through one point in the back focal plane is needed to form an image. In the back focal plane all the rays entering a given point are scattered by the specimen with the same angle. By inserting an objective aperture in the back focal plane where all the rays scattered from the specimen meets, determines the two imaging modes. When the position of the objective aperture to pass only transmitted electrons we get a BF image and the aperture is positioned to pass only diffracted electrons to form a DF image. Figure 15 the diagram representing to form a BF image.
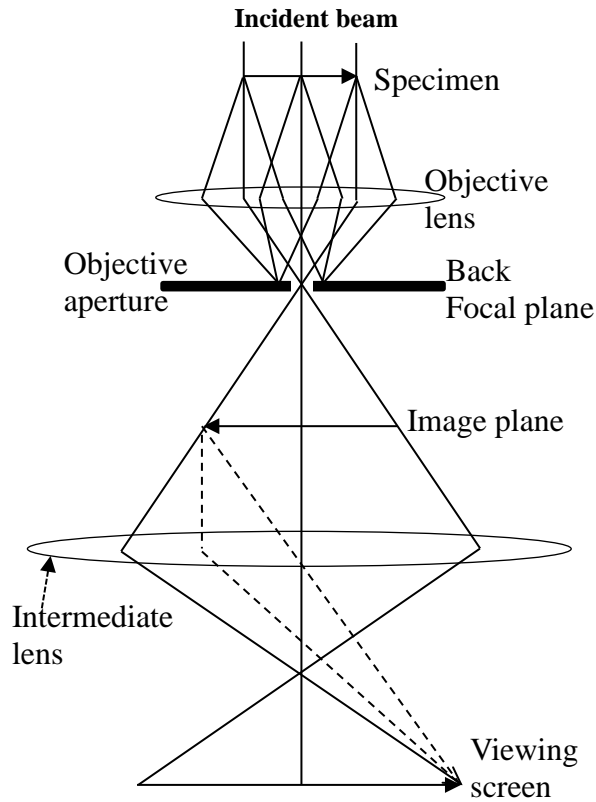
Figure 15 *BF Imaging mode, when the position of the objective aperture to pass only[11]*

In crystalline materials the feature can be clearly distinguishable by diffraction contrast; it is the variation in the intensity of the electron diffraction across the specimen. We can observe the diffraction contrast by inserting an objective aperture in the beam, so that the image is clearly visible and features are distinguishable. Without an objective aperture both the transmitted and diffracted rays leaves the specimen will recombine, suppresses the observed diffraction contrast and the image will be grey and featureless. There are two types of DF techniques dirty dark field figure16 (a) and axial dark field figure16 (b). In figure 16(a) spherical aberration is more, that is the electron trajectories that far away from the optic axis bent more strongly by the magnetic lens. In order to avoid bending and make high resolution DF image, it is better to tilt the incident illumination on the specimen. Figure 16(b) only the rays that diffracted from the right side is used for the DF image, the

transmitted beam is tilted into the position of the diffracted beams from the left on the back focal plane. This technique is called axial dark field imaging.
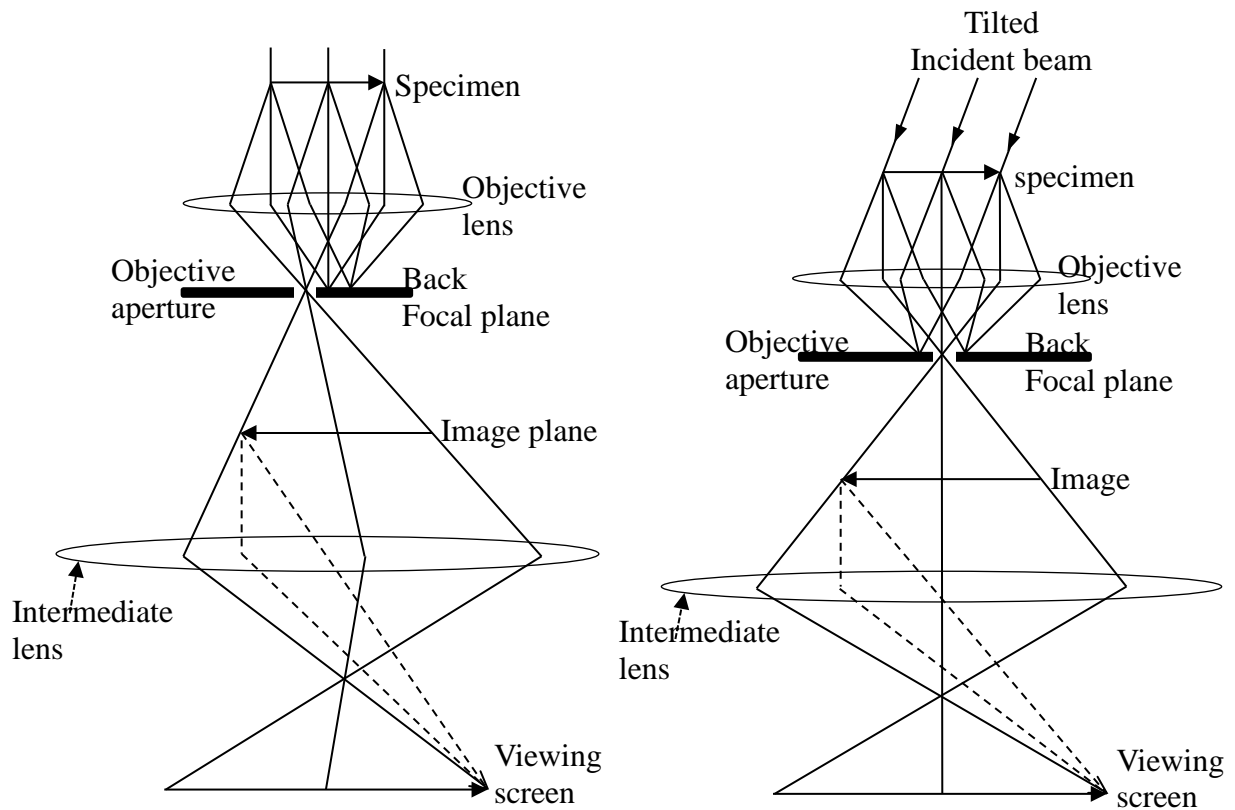
Figure 16: (a) Dirty dark field mode, spherical aberration is more, which the electron trajectories that far away from the optic axis bent more strongly by the magnetic lens. (b) Axial dark field mode only the rays that diffracted from the right side is used for the DF image, the transmitted beam is tilted into the position of the diffracted beams from the left on the back focal plane to get high resolution DF image[11].

Selected Area diffraction

The proper positioning of the objective aperture changes the modes of imaging in microscopes. Fig (17) shows the formation of diffraction pattern, an intermediate lens focused on the backfocal plane of the objective lens, allows both the transmitted and diffracted rays. In imaging mode we need to examine our specimen first until an area of interest is found. Then insert an intermediate aperture called selected area aperture is positioned around our area of interest in the specimen, switched into the diffraction mode, so that we can get a selected area diffraction (SAD) pattern from the region of interest in the image mode. This was invented by Le-poole in 1947. The technique of SAD is that when we insert an intermediate aperture in the image plane results the creation of a virtual aperture in the specimen plane. Only electrons falling the dimension within the virtual aperture in the specimen is allowed to pass into the imaging system. Rest of the electron beam hits the SAD diaphram.

Figure 17: SAD pattern only electrons falling the dimension within the virtual aperture in the specimen is allowed to pass into the imaging system.[11]

43

Lattice Imaging at High Resolution.

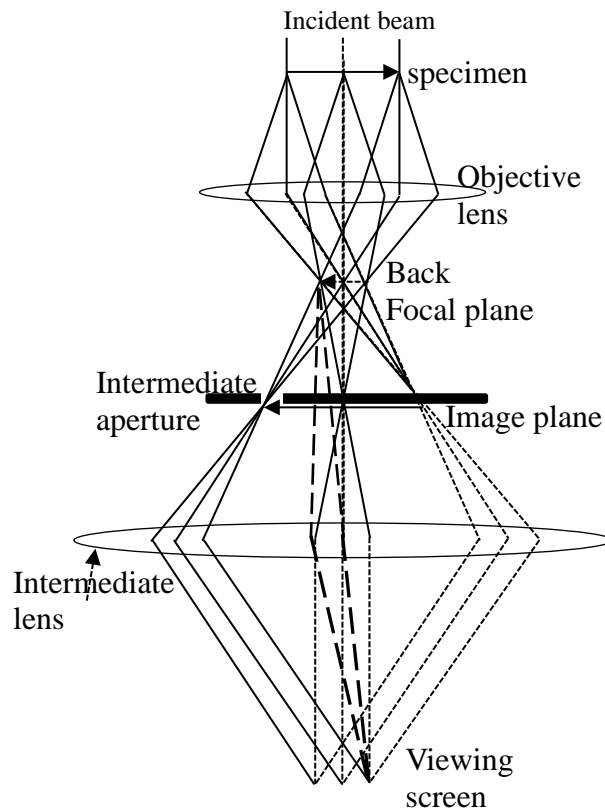High resolution imaging is used to study the atomic arrangements at interfaces, individual defects in crystals etc. From high resolution images we can see white spheres on a dark background and vice versa. These images are interference patterns between un-scattered electron waves and diffracted waves. We can understand the technique of high resolution through Fourier transforms. The electron wave function of the diffracted wave is the Fourier transform of the scattering factor distribution in the specimen $\rho(r)$ and the shape of $\rho(r)$ determine the atomic distribution in the specimen. The Fourier transform of the distribution of atoms in the specimen $\rho(r)$ is represented by $F[\rho(r)]$ is;

$$F[\rho(r)] = \frac{1}{\sqrt{2\pi}} \int_{-\infty}^{+\infty} \rho(r) e^{-i\Delta k.r} d^3r \ldots\ldots\ldots\ldots\ldots\ldots\ldots\ldots\ldots\ldots\ldots\ldots\ldots(32)$$

Where Δk is the Fourier transform function of the diffraction vector represents the periodicities in the specimen. In TEM the Fourier transform of the specimen is truncated by an objective aperture which is located in the back focal plane of the objective lens. The equation that relates the smallest spatial feature in the image Δx by an objective aperture at a particular range in terms of k - vectors δk is;

$$\Delta x = \frac{2\pi}{\delta k} \ldots\ldots\ldots\ldots\ldots\ldots\ldots\ldots\ldots\ldots\ldots\ldots\ldots\ldots\ldots\ldots\ldots\ldots..(33)$$

In order to resolve the atomic periodicities we need an objective aperture that incorporates a range $\delta k \cong \frac{2\pi}{d}$, where d is the atomic separation in the specimen. The objective aperture should be large enough to include at least one diffracted beam and the transmitted beam.

2.9.6 Moiré fringes

Moiré' patterns are kind of double diffraction commonly seen in materials occurs when two different grains or crystals overlap along the direction of beam. In this case each diffracted beam from the first crystal will turn into an incident beam for the second crystal. There are different situations arises according to the periodic matching of the lattice planes, the interplanar distance, reciprocal lattice vector between the two crystals along the interface. For example two crystals A and B by a set of lattice planes with interplanar distance d_1 and d_2 with reciprocal lattice vectors g_1 and g_2, the three different situations arises are;

(1) The reciprocal lattice vectors are parallel but have different length, in this case the difference in vector $\Delta g = |g_1 - g_2| = \frac{d_1 - d_2}{d_1 d_2}$ and we can observe fringes in the image with fringe spacing D is given by $D = \frac{d_1 d_2}{d_1 - d_2}$ and these type of fringes we observed are called parallel fringes because fringes are parallel to both sets of planes and perpendicular to the difference vector Δg.

(2) The reciprocal lattice vectors have same length but slightly rotated by an angle β , therefore the spacing between the fringes $D = \frac{d}{\beta}$. The observed fringes are perpendicular to each other. These are called rotational moiré fringes. Figure (18) shows an example for this type.

(3) If the lengths are different with a rotation β

the fringe spacing is $D = \frac{d_1 d_2}{\sqrt{(d_2 - d_1)^2 + d_1 d_2 \beta^2}}$, the fringe spacing are again perpendicular to the difference vector Δg .

These two overlapping crystals also produces a composite diffraction pattern consists of two spots which are separated by a slight distance Δg in reciprocal space. We can also measure the lattice plane mismatch of the two crystals by measuring the spacing between the moiré fringes.
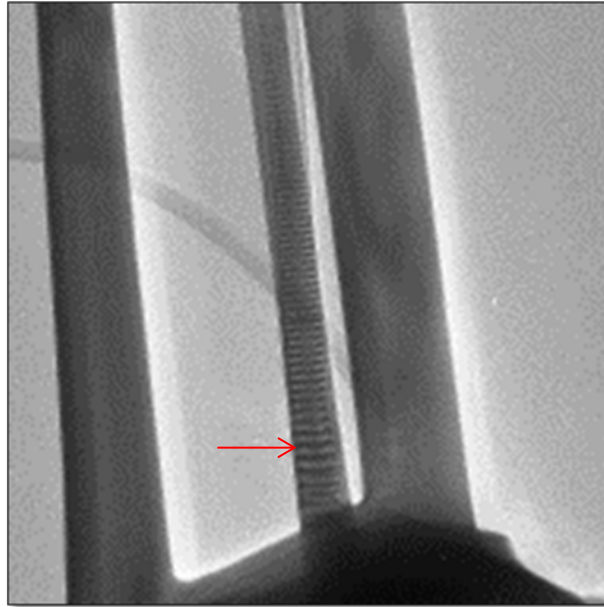
Figure 18*: Moiré pattern arrow in figure, crystals overlap along the direction of beam and the reciprocal lattice vectors have same length but slightly rotated by an angle β forming this moiré pattern.*

2.9.7 Thickness fringes and Bend Contours

We can explain the thickness fringes with the help of Howie-Whelan equation which gives the intensity in the Bragg-diffracted beam I_g is that,

$$I_g = |\phi_g| = \left(\frac{\pi t}{\xi_g}\right)^2 \left(\frac{sin^2(\pi t s_{eff})}{\pi t s_{eff}}\right) = I - I_0 \dots\dots\dots\dots\dots\dots\dots\dots\dots\dots\dots.. (34)$$

Where ϕ_g is the amplitude of the diffracted beam, t is the distance travelled by the diffracted beam, ξ_g is the extinction distance is the characteristic length for the diffraction vector g which depends on the lattice parameters, atomic number and wavelength we used, s_{eff} is the effective excitation error and I_0 the incident beam intensity. Equation (34) tells that the intensity of the incident beam I_0 starts equal to unity and decays gradually. But the intensity of the diffracted beam I_g gradually increases until it becomes unity. This kind of oscillations in I_g and I_0 are called thickness fringes. Thickness fringes are mostly observed

in wedge shaped TEM specimens, so that we can see a set of alternating light and dark bands. Figure 19 shows an example for thickness fringe. We can observe thickness fringes in the thinner region of the specimen and becomes less visible when it reaches the thicker region of the specimen. This means that intensity between bright and dark bands varying at the thinner and thicker region of the sample. In the thinner region the amplitude and intensity of the diffracted wave increases linearly related with the thickness of the sample. When moves towards the thicker region of the specimen the intensity of the diffracted beams are out of phase. This is an absorption effect which means that unit cells located at the thinner region receive stronger incident beam, increase the average amount of scattering so that we can see very dark bands.
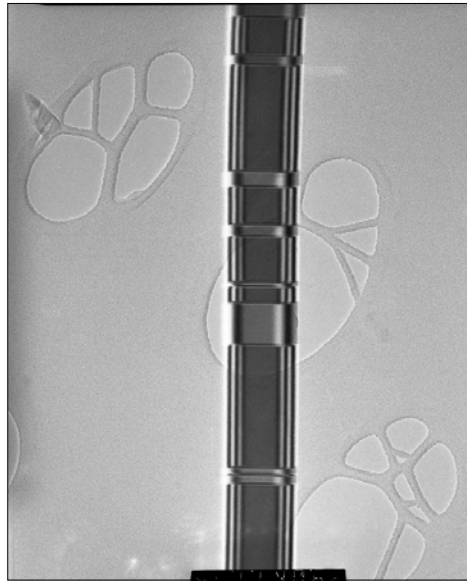
Figure 19: Thickness fringe due to the variation of intensity between bright and dark bands at the thinner and thicker region of the sample forming a set of alternating light and dark bands.

Bend contours are diffraction contrast effects where the specimen thickness is constant, but the specimen is bent, so that bend contours is formed as broad, fuzzy dark lines in BF images. The same family of atomic planes will not be equally oriented when the specimen is bending, so that it is impossible for all regions of the specimen to be in the same diffraction condition at same time.
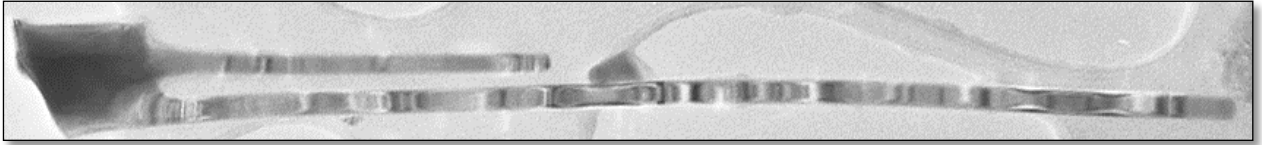
Figure 20: *Bend contour occurs when the specimen is bend forms fuzzy dark lines can be seen in this figure.*

2.9.8 Molecular beam epitaxy (MBE).

MBE is one of the most widely used techniques for growing thin, epitaxial films of different materials. The materials are deposited on a substrate by evaporating the material from the effusion cells in a chamber which is maintained under ultra-high vacuum. The MBE machine used for nanowire growth in this study is Varian Gen II Modular system. The growth chamber is the major part of the MBE machine, whose schematic representation is shown in figure 21(a). The growth chamber consists of ion pump, a titanium sublimation pump, Cryopanels cooled with liquid nitrogen and glycol cooling of the source flange. The different effusion cells installed in this particular MBE are As and Sb valved cracker cells, dual filament Ga, Al, and In cells and three doping cells of Si (n-type), GaTe (n-type) and Be (p-type). The flux emitted from the effusion cells can be measured with the help of an ion gauge. The Reflection high energy electron diffraction (RHEED) in this set up consists an electron gun, emits an electron beam with tunable energy which is used to record the symmetry of substrate surface with material during the growth. Continuous azimuthal rotation (CAR) system provides the rotation of substrate during the growth.[15]

RHEED-gun

Cryopanels

Ion Gauge

4 Effusion cells

CAR

Fluorescent Screen
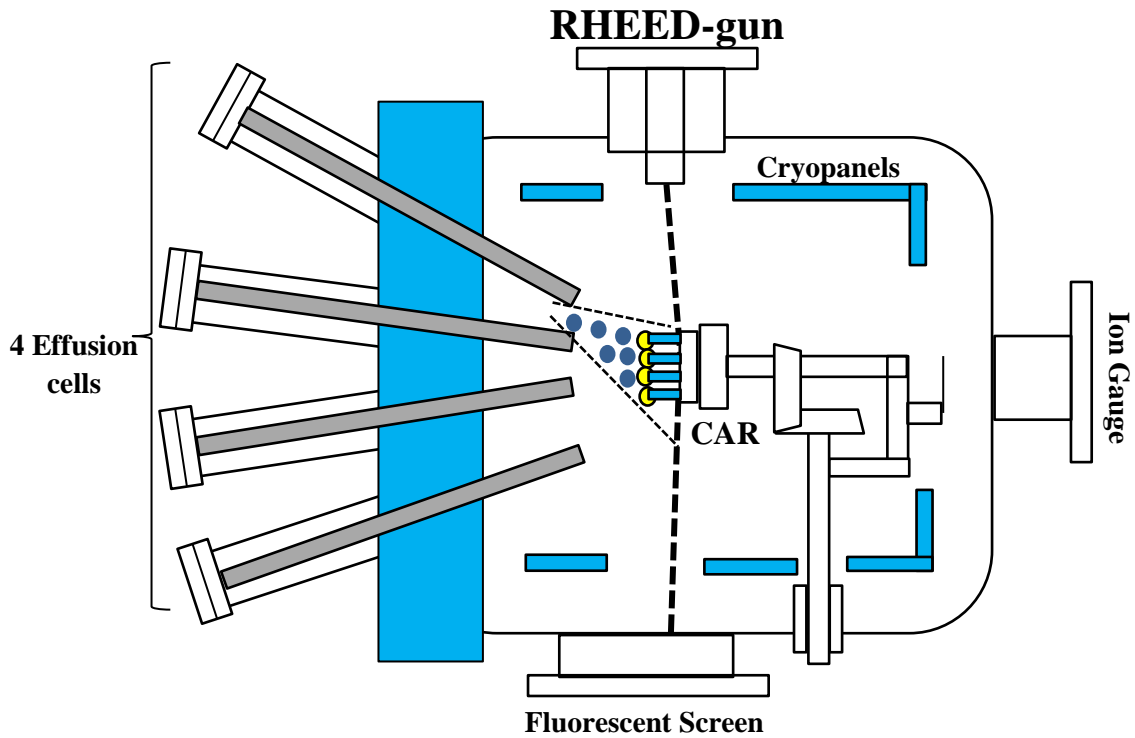
Figure 21(a): *Schematic representation of MBE growth chamber at NTNU* [15]

2.9.9 Vapour-Liquid-Solid (VLS) mechanism.

VLS mechanism was first demonstrated by Wagner and Ellis in 1964 for the fabrication of NWs. In this technique we often use Au as a catalyst, which forms a liquid-alloy particle when it reacts with source materials supplied in vapor form. If we continuously supply the source material to the liquid-alloy, the source material dissolves in the liquid-alloy until the composition reaches the liquidous line. When we supply the source material beyond the liquidous line, the source material dissolves but segregates from the alloy and precipitates in the form of solid NW at the bottom of the particle. The nanoparticles are randomly distributed, so that the NWs are positioned randomly on the substrate. This technique allows us to tailor the composition of heterostructured NWs in both radial and axial directions.[15]

49

2.9.10 Doping in Semiconductor Materials.

Semiconductors are group of materials having electrical conductivities in between insulators and metals. The energy band gap is one of the most important characteristics of semiconductors, which distinguishes it from metals and insulators. The electrical conductivity of these materials can be varied by making changes in temperature and optical excitation. By impurities, temperature dependent can be taken out and large difference in conductivity can be obtained by controlled way of changing doping concentration. This makes the semiconductor materials are natural choices for the manufacturing of various electronic and optoelectronic applications. This addition of controlled amounts of impurities strongly affects the optical and electronic properties of semiconductor materials and the process of controlled addition of impurities for varying the conductivity is called doping. Main charge carriers for conduction in the semiconductor materials are positively charged holes and negatively charged electrons. By doping, a crystal can be changed so that it has a prevalence of either electrons or holes, so that there are two types of doped semiconductors formed, p-type (mostly holes) and n-type (mostly electrons). These types of doped materials are called extrinsic materials. In crystalline materials the allowed energy states of electrons are described by a set of allowed bands separated by forbidden band gaps. In semiconductors the band that is filled with electrons at 0K is called the valence band and the unfilled upper band is called the conduction band. Therefore in semiconductors the number of electrons or holes available for conduction can be increased greatly by optical or thermal energy. While discussing electronic devices from n-type and p-type semiconductor materials the importance of doping will become obvious and when a semiconductor is doped n-type or p-type one type of carrier electrons or holes dominates.[16]

When impurities are introduced into a crystal, within the band gap, additional energy levels are created in the energy band structure. In n-type semiconductor material, for example an impurity from column V of the periodic table introduces an energy level very close to the conduction band and this level is filled with electrons at 0 K. To excite these electrons to the conduction band some thermal energy is needed and all of the electrons in the impurity level are donated to the conduction band. Such an impurity level is called

donor level and impurities are called donor impurities. This kind of materials with electrons as majority carriers is called n-type material. In the case of n-type materials, for example atoms from column III of the periodic table introduce an impurity level near the valence band and these levels are empty of electrons at 0K. At low temperature enough thermal energy is required to excite electrons from the valence band to the impurity level, leaving behind holes in the valence band. This type of impurity level accepts electrons from the valence band called acceptor level, so that doping with acceptor impurities creates concentration of holes much greater than the electron concentration in the conduction band. This type of materials with holes as majority carriers is called p-type material.

Most of the semiconductor devices contain at least one junction between n-type and p-type material, the so called p-n junctions which are used for the various operations in electronic circuits such as amplification, rectification, switching etc. The doping concentration on each side of the junction determines many of the properties of the junction which is very important for the fabrication of various electronic device applications. In biased p-n junctions current flows freely which can be used for various applications in electronic devices such as photocells, light emitters etc. When p-n junctions are formed within single semiconductors are called homojunction whereas junctions between two lattice matched semiconductors with different bandgaps are called heterojunctions, for example GaAs-AlGaAs . These heterojunctions opens a wide range of possibilities for device applications such as semiconductor lasers, field effect transistors etc. Nanowires are such types of heterostructures and control of the doping in NW based semiconductors is essential for realizing a wide range of optoelectronic devices.

2.9.11 Material system and NW growth Mechanism.

Gallium Arsenide is a III-V compound semiconductor with lattice constant of 5.65325 Å, used for manufacturing electronic and optoelectronic devices. III-V refers to the group in the periodic table where Ga and As belongs to with atomic number 31for Ga and 33 for As respectively. GaAs is a direct bandgap material with bandgap of 1.424 eV, its excellent optical properties make it as a very good candidate for optoelectronic devices. Berillyum (Be) atomic number 4, and is a p-type dopant in III-V compound semiconductors. For

example complex layered structures of GaAs in combination with Be or the alloy GaAs $_{1-x}$ Be$_x$ can be grown by Molecular beam epitaxy (MBE).

We can fabricate heterostructured NWs in different possible directions. The tiny size of NWs allows growing heterostructures involving materials with large lattice mismatch, which provides the provision to relax in the radial direction without forming any misfit locations. [15]The heterostructures in NWs allows growing either in axial direction, radial direction or both as shown in figure 21(b).

Axial   Radial   Axial and Radial
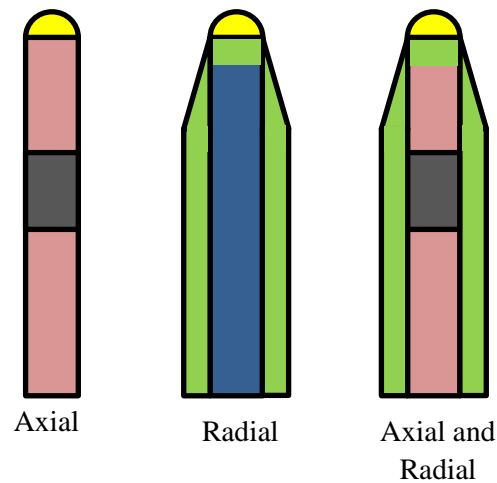
Figure 21(b) Schematic representation of heterostructured NWs allows growing in different possible directions.

The NWs grown on MBE by which the constituent atoms are supplied in the form of adsorbed atoms or adatoms rather than metal-organic groups. In Au-assisted NW growth, the role of Au as a catalyzing agent to decompose the metal-organic groups and the Ga adatoms diffuse from the substrate surface to the NW base and then to the Au particle. During the NW growth, firstly the Au particle deposited on the GaAs (111)B substrate. While heating the substrate at a particular temperature the Au particle dissociates into nanoparticles and reacts with the Ga from the substrate surface forming a liquid Au-Ga alloy. By continuous supplying of Ga to the substrate, the Ga adatoms can impinge directly on the Au particle along with the NW side wall. When the Ga composition in the Au-Ga alloy reaches the solubility limit, the excess Ga in the Au-Ga alloy segregates and

precipitates at the Au-NW interface and forms the GaAs NW by reacting with the available As atoms around it. When the NW grow longer, tapering (more growth on the NW side facets) of the NW can be observed. This is because when the length of the NWs exceeds the diffusion length of the Ga adatoms the initiation of radial growth on the NW sidewalls starts to increase. The VLS mechanism allows tailoring the composition of NW in both the axial and radial directions. If the substrate temperature is increasing the NWs have a chance to grow radially than axially, such that the decomposition rate of metallic groups at the NW side is equal or higher than the Au particle.[15]

Chapter 3

Experimental Techniques

3.1 Growth details of four different batches of nanowires.

   The nanowires investigated in this study were grown by Dheeraj Dasa and Mazid Munshi at the Department for Electronics and Telecommunications at NTNU. Be doped GaAs NWs were grown by Ga and Au assisted VLS techniques in a VarianGenModular MBE system equipped with Ga dual-filament cell, As valved cracker cell and Be effusion cell, allowing to fix the proportion of As dimers and tetramers. The NW growth were carried out on p-type doped Si (111) and GaAs (111)B substrates for Ga and Au -assisted techniques respectively.

(a)   As605-2 and As605-3 :

   Be -doped GaAs NWs were grown GaAs (111)B substrates using Au -assisted MBE technique. A nearly 3 Å thick Au film was deposited on the substrate and then loaded in the MBE machine. When the substrate was heated at an elevated temperature with an As flux of $5.6x10^{-6}\,Torr$, which resulted in the formation of Au-Ga alloy. Then the substrate temperature was reduced to the growth temperature of 510^0 C, which is suitable for GaAs NW growth. The Ga cell temperature was set to produce a nominal planar growth rate of 0.7ML/s as measured on GaAs (100) substrate. The NW growth was initiated by opening the Ga and Be shutters, and the growth was continued for 35min. Two samples were grown with two different Be concentrations which are equivalent to $8.36x10^{18}cm^{-3}$ for As605-2 and $1.2x10^{19}cm^{-3}$ for As605-3 on GaAs thin film. The growth of these NWs was initiated by opening the shutters of Ga and Be effusion cells and the termination was done by shutting down the Ga, Be and As fluxes simultaneously.

(b)   SC-95 and SC-169:

Two Be -doped GaAs NW sample were grown on Si (111) substrate using Ga -assisted MBE technique. The NW growth was initiated by opening Ga, As and Be shutters simultaneously, and the growth was continued for 40min and the termination was done by shutting down the Ga, As and Be fluxes simultaneously. The Ga rate was 0.7ML/s and As flux was $5.4x10^{-6}\ Torr$. The planar equivalent Be concentrations were $3.5x10^{18}cm^{-3}$ for SC-95 and $1.17x10^{19}cm^{-3}$ for SC-169. The substrate temperature was 640^0C during the entire growth.

Table 3 growth parameters of four different NW batches.

NW	Substrate	Catalyst	Ga-rate	As-flux Torr	Be cm^{-3}	Be Temperature Celcius
As605-3	GaAs(111)B	Au	0.7 ML/s	$5.6x10^{-6}$	$8.36x10^{18}$	1165,35 min
As605-2	GaAs(111)B	Au	0.7 ML/s	$5.6x10^{-6}$	$1.2x10^{19}$	1075,35 min
SC-95	Si(111)	Ga	0.7 ML/s	$5.4x10^{-6}$	$3.5x10^{18}$	995, 40 min
SC-169	Si(111)	Ga	0.7 ML/s	$5.4x10^{-6}$	$1.17x10^{19}$	1075, 40min
SC-50	Si(111)	Ga	0.7 ML/s	$5.4x10^{-6}$	1.4×10^{18}	995, 40 min

Note: "The batch SC-50 gave similar results as batch SC-95 and so it will not be presented in this report".

3.2 Sample preparation for TEM characterization.

(a)   **(b)**   **(c)**
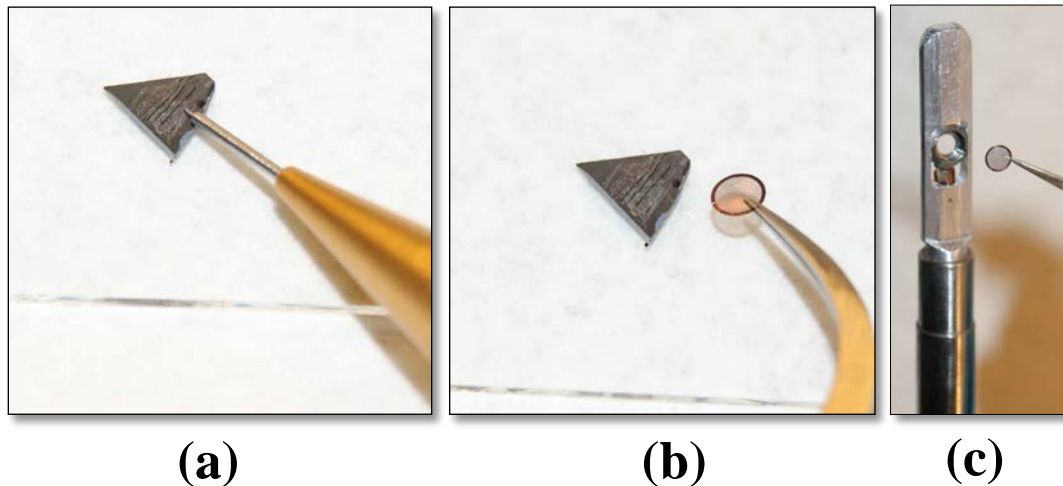
Figure 22: The step by step micro-cleavage technique of sample preparation for TEM.

(a) The NW after growing appears as a dark layer on the substrate and glue it on a glass plate. Pour a drop of isopropanol on it and scratch the wafer by using a diamond scribe. The direction of the scratching was selected in between the cleavage planes of the wafer. This is called micro-cleavage technique which is very good for getting a sample along with its substrate which is necessary for substrate interface structural characterization. This technique is relatively simple and the micro cleaved sample is well suited for rapid crystallographic orientation and determination in the TEM.

(b) After cleaving, mechanically transfer the sample on a 300 mesh copper grid, so that the NW is lying on the mesh for TEM investigation. The role of isopropanol is to well disperse the NWs on carbon mesh.

(c) Inserting the specimen on a double tilt TEM specimen holder for characterization.

3.3 TEM Characterization of Nanowires

For TEM characterization of NWs Philips CM30 a 300 kV microscope with LaB_6 was used. Microscope was operated at a high tension of 200 kV for nanowire characterization. A double tilt sample holder was used for inserting the NW specimen to the microscope. The BF, DF and high resolution images from the NW were captured by either film or by a 1k Tietz CCD camera. The entire diffraction pattern from the specimen were captured on film and developed. The negatives were scanned with a resolution of either 300 or 600 dots per inch (dpi).

3.4 Software for data processing

The following three software packages were used in this study.

EM-Menu ver 4 is a software package from Tietz Video and Imaging processing systems. It was used to acquire and process the images from the CCD camera on the Philips CM30 TEM.

Digital Micrograph, from Gatan Inc. is a software package for to analyze and process the images from TEM. This is a very useful tool for adding scale bar on the scanned images by calibrating negatives and images from CCD. The crystal structure from the high resolution images can be determined by selecting the region of interest in the image and then perform Fast Fourier Transform (FFT) from the same region.

Jmol, is a free ware program written in Java for drawing crystal structure, which was used for drawing ZB and WZ crystal structure.

All the figures and diagrams (except figure 40) in this thesis were prepared in Microsoft PowerPoint.

Chapter 4

Results

In this section a detailed description of four different batches of NWs, containing two Au-assisted GaAs nanowires on GaAs (111)B substrate doped at different Be concentrations and growth parameters and two self-catalyzed that is Ga-assisted GaAs nanowires on Si(111) substrate doped with different Be concentrations. Different TEM techniques like BF and DF imaging, High resolution imaging and SAD have been used for the structural characterization of the nanowire batches. In this study the main aim is to determine the crystal structures, twin phase boundaries, and stacking faults in combination with SAD and lattice imaging of nanowires which gives a good representation of the NW samples. To ensure reproducibility and consistency at least five NWs from each batch were examined in detail. NWs were screened for stacking faults and twin defects over their entire length. The different TEM results will be present and discussion of them will be given in the next chapter. ***Note: SAD patterns are taken in [110] and [11$\overline{2}$] zone axis direction.***

4.1 Nanowire batch I (As605-3)

Figure 23 shows the BF overview image of the vertically grown high density of NW group grown by Au assisted VLS technique. However, in this study very little variation in the height of the NWs with their diameters can be observed. On the substrate surface a small pyramid like formation (red arrow indicated in Figure 23) along with the NWs. Since this NW is Au-assisted, gold droplet can be seen at the top of the wire and also few stacking faults (red arrows shown) can be seen in the long thin ones than the thicker NWs.
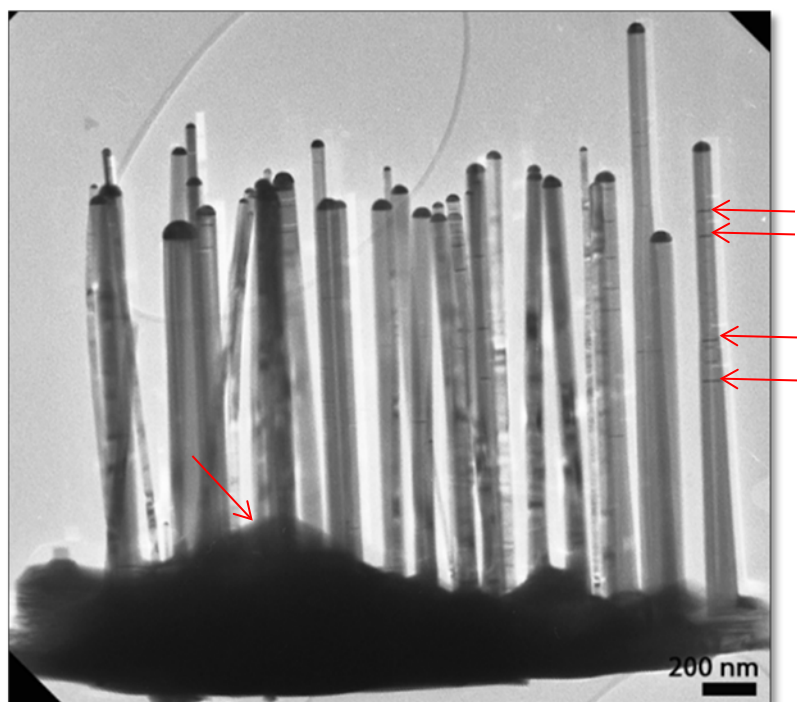
Figure 23*: An overview image of NW group along with the substrate from batch I. The image gives an impression of the NW morphology.*

In figure 24 (a) and (b) BF images of two different NWs from the same batch, the wires are vertical, rod-shaped with even in diameter and hardly any stacking faults seen in the thicker NW but few twinning can be observed in the top of the thinner NW. The Au nano particle looks like a semicircle located at the top of the nanowire. The indexed diffraction pattern figure 24(c) corresponding to the BF image of the thicker NW is in [111] growth direction. From this direction the NWs seems to be perfectly straight and twin planes could not be observed. The other diffraction patterns that observed form this particular NW batch (thicker and the thinner NWs) cannot be indexed because the ratios and angles measured cannot be matched to candidates ZB or WZ.
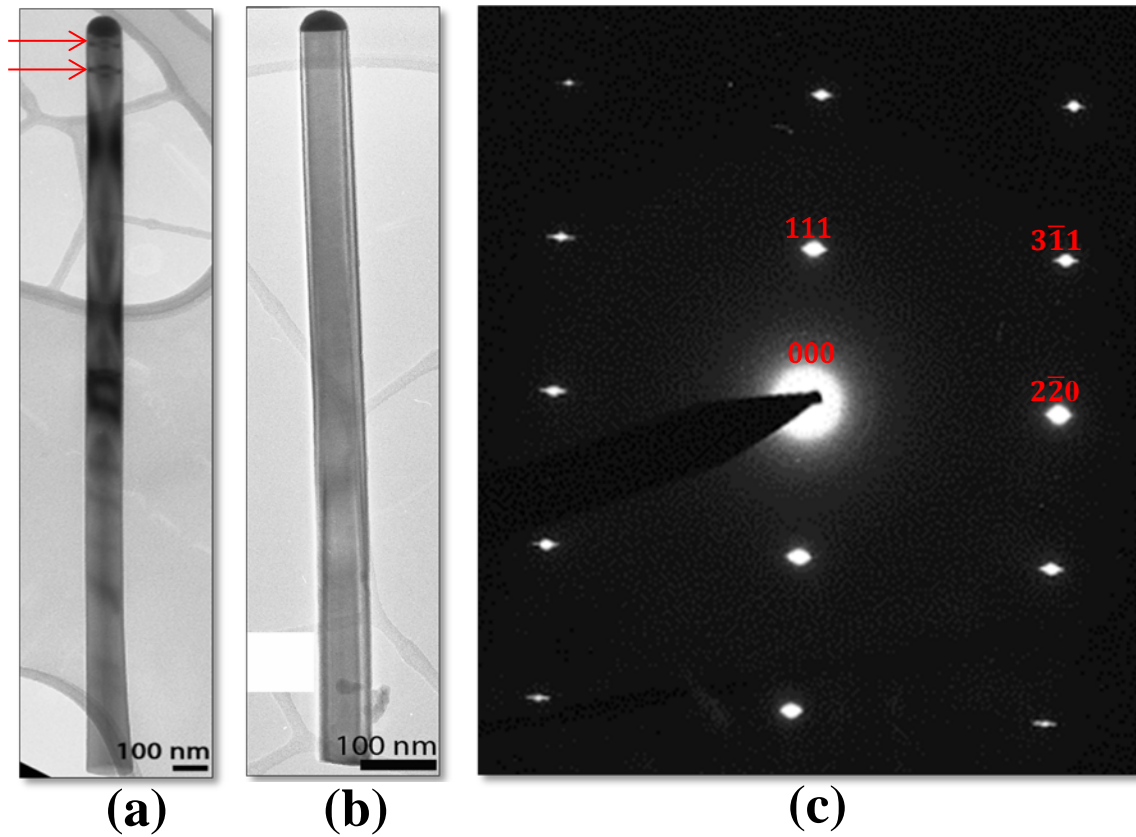
Figure 24: *(a) and (b) BF images of the two different NWs (one thin and thick NW) from batch I. Red arrow in (a) indicates the small defect in the NW top. (c) SAD pattern from thicker NW (b) in [111] growth direction.*

In figure 25(a) shows a cleaved off substrate-interface piece with NWs attached. In the image actually four different nanowires, two of them lying one behind the other and the reciprocal lattice vectors have same length but slightly rotated by an angle, forms a moiré pattern (arrow shown in the figure). This is not a stacking fault.

(a) **(b)**
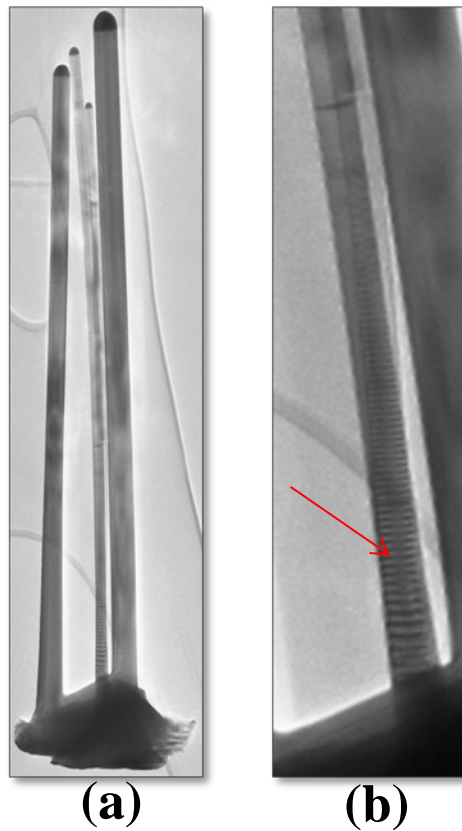
Figure 25: *(a) Four NWs along with substrate and two of them lying one behind the other to form Moiré pattern. (b) A close up view of the Moiré pattern.*

In figure 26 the BF image of the NW substrate interface from NW batch I and SFs are observed at the interface region and the corresponding diffraction pattern from the interface seems to be ZB with twinning. Red circle in figure 26 (a) shows the place where the SAD pattern was taken.

(a)   **(b)**
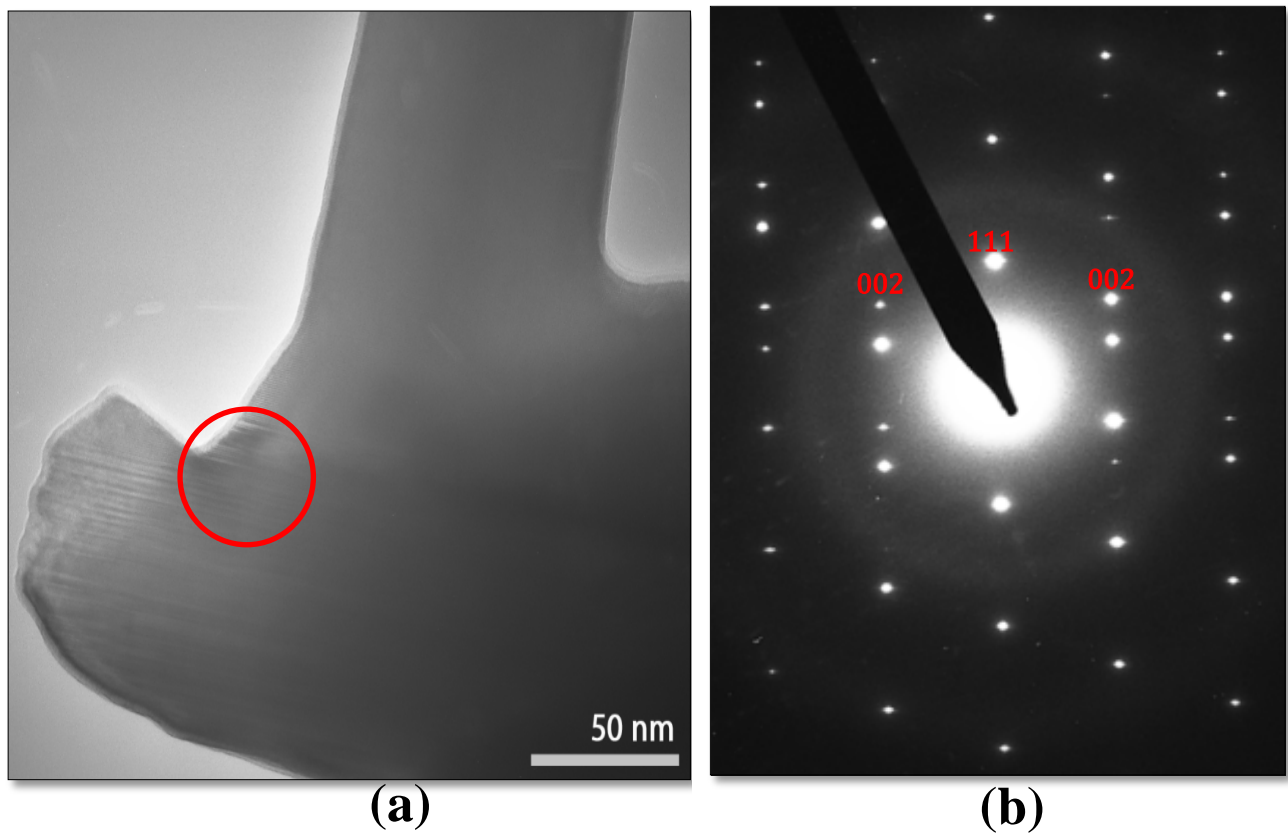
Figure 26: (a) BF image of NW substrate interface from batch I, red circle indicates the place where SAD pattern taken. (b) SAD pattern from the corresponding NW substrate interface indexed as twinned ZB crystal structure.

4.2 Nanowire batch II (As605-2)

Figure 27(a) showing the BF overview image of Be-doped GaAs NW group grown by Au assisted VLS technique on GaAs (111)B substrate. In this NW batch, the doping concentration of Be is comparatively higher than the NW batch I. The wires seems to be thicker at the bottom and decrease in the diameter when it growing to the top. A pyramid like formation is seen on the substrate surface (indicating by red arrow) and NWs are attached to it. Since this NW is Au-assisted, gold droplet can be seen at the top of the wire which is vertical on the substrate. Figure27 (b) A close up view of the Au-droplet tip and a particle inside the Au droplet was observed shown by red arrow in the figure. The assumption is that there are two phases in the Au droplet (the particle inside the Au droplet). In further "more work is needed to find out what".
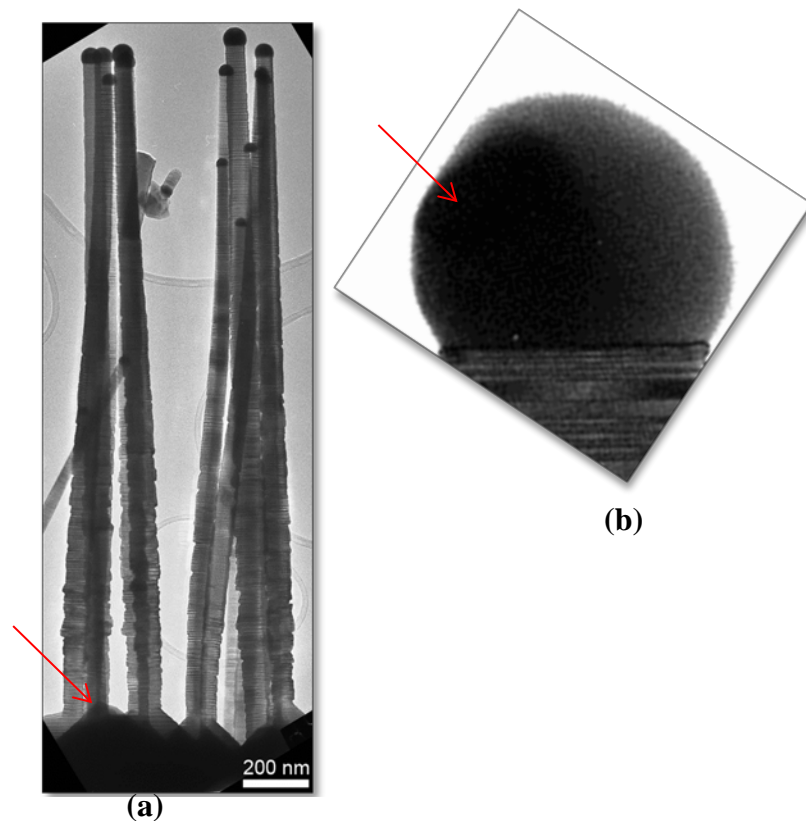

Figure 27: (a) BF overview image of NW group along with substrate from batch II. Red arrow indicates the pyramid like formation at the NW substrate interface. (b) A close up view of the Au-droplet tip, a particle inside the Au droplet can be seen shown by red arrow.

Figure 28 an overview TEM BF image of Be doped GaAs NWs grown by Au assisted VLS techniques. According to the NW morphology, randomly distributed high density stacking faults (SFs) from bottom to top and the twin planes have both uniform and non-uniform spacing were observed. The NWs are tapered, grown both radially and axially. In addition to these, highly anisotropic overgrowth can be observed on the NW side facets in (111) B direction. The additional overgrowth seems to be decreased from bottom to top of the NW; this means that the additional overgrowth is very high in the NW bottom part. Overall this NW having very high density of rotational twins with randomly distributed stacking faults and additional overgrowth on NW side facets. The crystal structure from the different segments can be deduced by using SAD patterns as well as high resolution TEM images. Figure 28(c) and (d) shows the indexed diffraction pattern from the corresponding BF nanowire, from the SAD pattern the crystal structure of Be-doped GaAs NW grown by Au-assisted technique can be indexed as the NW adapts a predominantly ZB crystal phase with a high density of rotational twins in the [111] NW growth direction. ***Note: The twinning of two crystals [indicated by blue and red color in figure 28(d)] is because of the single (111) atomic plane around which the crystal structure is rotated by 60^0 and the rotation of the corresponding diffraction pattern results in a characteristic double spot pattern. This is same for all the twinned ZB diffraction patterns in this study.*** The additional spots in the SAD pattern figure 28(d) is because of the bottom part is very thick and we get reflections from all [111] directions which is clearly shown in figure 29 (f) and (g).
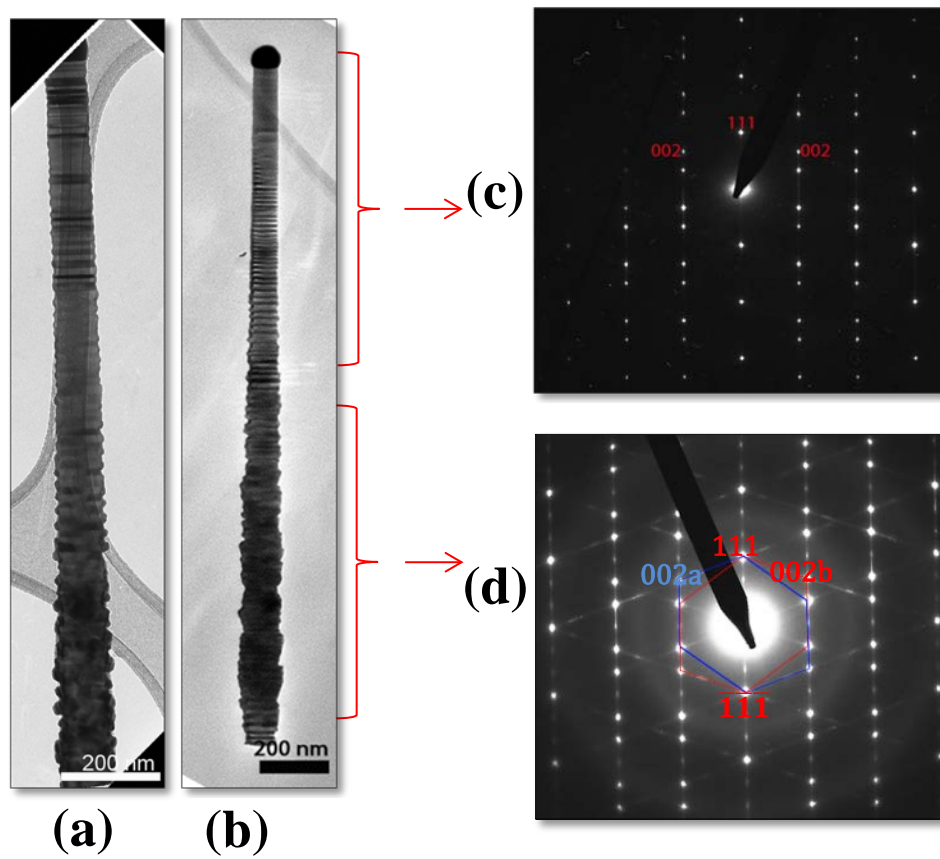
Figure 28*: (a) and (b) BF images of two different NWs from batch II. (c) and (d) SAD patterns from top to middle and middle to bottom part of the NW indexed as ZB with twinning.*

Figure 29 showing a closer look of the NW, divided into three segments and all are not from the same single NW. In Figure 29 (a) part1 that is from the top of the NW, very interestingly, the catalyst droplet diameter is bigger than the NW diameter. It is very clearly seen that randomly distributed stacking faults with rotational twins in the NW. In part (b) and (c) in this particular segment we can very clearly seen the overgrowth on the NW sidewalls and the periodically arranged twin structure. Therefore twin planes that have constant spacing within a nanowire is called twinning super lattice (TSL)[10] were identified. The same TSL appears to be in different places in different NWs upon investigation by TEM. The last part (d), the very bottom part which is very thick, high twin defects, overgrowth on the NW sidewalls and high density of randomly distributed stacking faults.

Figure 29 (e) shows the SAD pattern from the top part figure29 (a) of the NW, the dominating structure is ZB with repeated twinning in the [111] growth direction and there is no extra spots in addition to the twinning spots visible in the diffraction pattern.

Figure 29 (f) the SAD pattern from the TSL image, this pattern have some extra spots (indicated by red circle in figure) and this is due to the reflection of diffraction spots from the overgrowth part on the NW side facets in (111)B direction. This particular segment is thicker so that we get the multiple scattering effects so that the reflections gain intensity and becomes more visible.

Figure 29 (g) the SAD pattern from the very bottom part which is the very thicker part with a very high twinning density in different [111]-directions. In this pattern the extra spots more visible in addition to the normal ZB twinnig spots red circle in figure29(g) is because of the reflection of planes from different [111] directions both from the NW and the overgrowth part on the NW side facets. Also the multiple scattering effect is more here and the additional spots are more visible because of the successive scatterings.
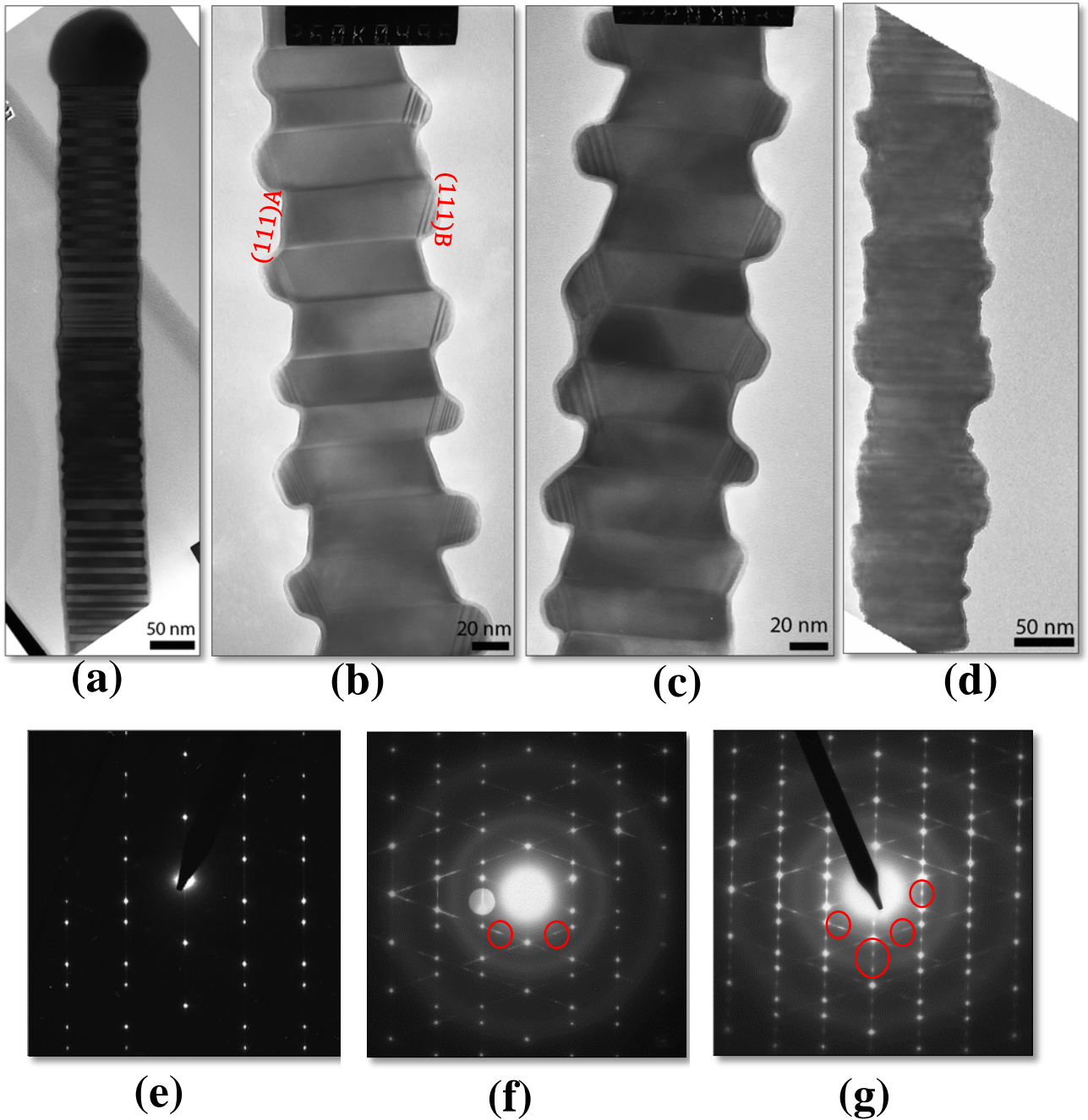
Figure 29: *BF images of different segments from NW batch II. (a) Top part of the NW. (b) and (c) Twinning super lattice (TSL) with NW overgrowth on side walls. (b) Very bottom part of the NW with randomly distributed high density twinning. and merged overgrowth on NW side walls. (e), (f) and (g) showing the difference in the diffraction patterns form the top, TSL and bottom part of the NW respectively.*

In figure 30 all the images are at same magnifications. (a) BF image of TSL segment by selecting the center diffraction spot. (b), (c), (d) and (e) DF images from the same segment by selecting four different (diffraction spots) (hkl) planes. Figure 30 (f) is also a dark field image by selecting the additional spot from the TSL diffraction pattern for to show the overgrowth on the NW side facets. So we see brightness on the overgrowth and other region appears dark. *Note: White circle in figure 29(f) selecting the diffraction spots [(hkl) plane] by positioning the objective aperture to get a DF image.*
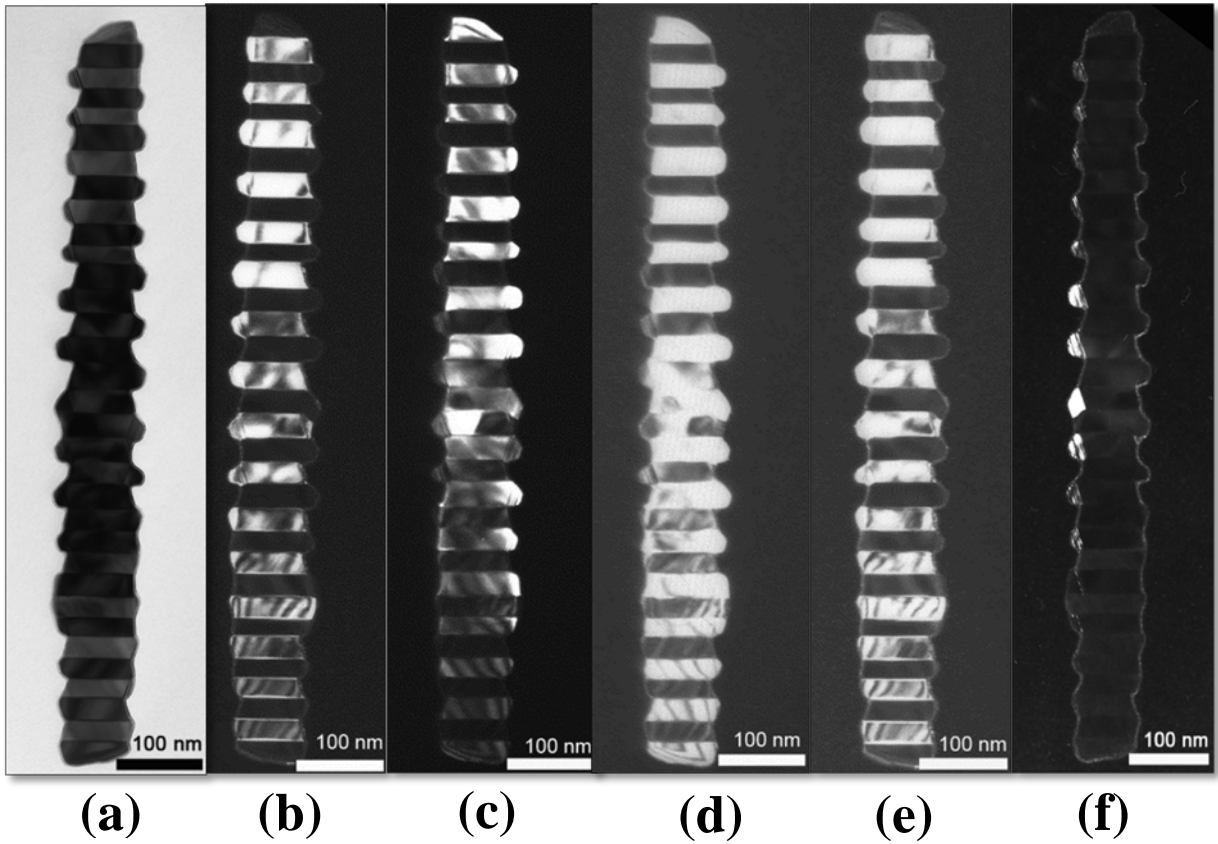
(a)   **(b)**   **(c)**   **(d)**   **(e)**   **(f)**

Figure :30: *(a)BF image and (b), (c), (d), (e), (f) are DF images by selecting different (hkl) planes from the SAD pattern, for to show the twinning density in the TSL structure and the additional overgrowth on the NW side facets.*

In figure 31 (a) and (b) a clear high magnification BF image of two different anisotropic overgrowth on the NW side walls which is grown in the (111) B direction. We can clearly see a high number of twin defects in the overgrowth part. In the HRTEM image it is clearly visible the ZB structure with the presence of twin plane and is confirmed from the Fast Fourier Transform (FFT). Figure 31 (d) a twin plane can see in both the NW and the overgrowth direction. FFT is taken from figure 31 (c) shown by red square.

(a)

(b)

(c)

(d)
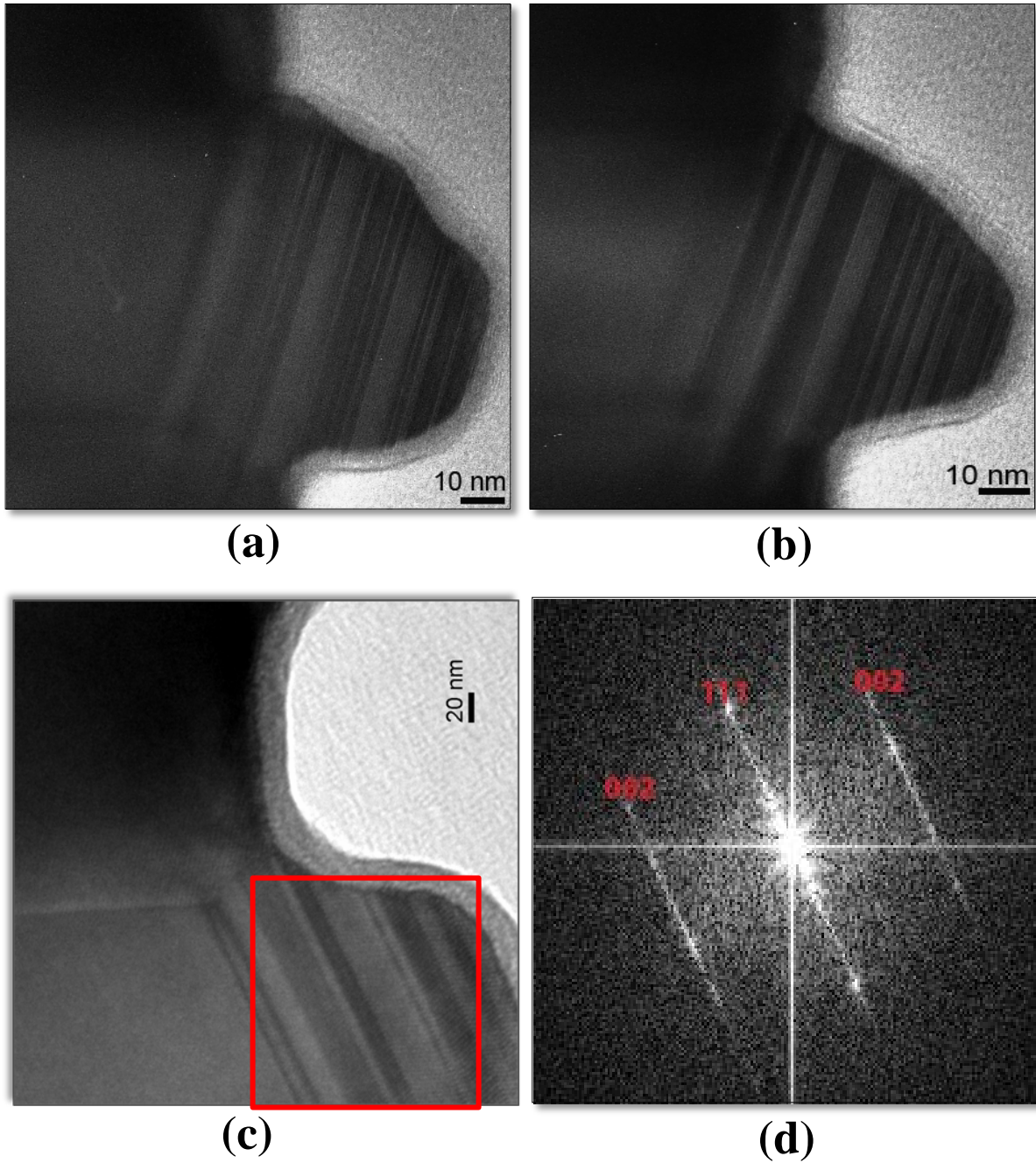
Figure: 31: (a) and (b) two different overgrowth on the NW [111] B direction. (c) HRTEM image from NW overgrowth, also NW twinning plane can be clearly visible. (d) FFT from NW overgrowth (red square) in figure (c) is identified as ZB with twinning.

Figure 32(a) BF image from a cleaved off substrate-interface piece along with a NW and we can clearly visible the high twinning density in the NW substrate-interface. The corresponding SAD pattern from the interface indexed as ZB with twinning. The streaks that is seen in the diffraction pattern is due to the finely twin structure in the NW which is normal to the electron beam (real space) so that diffraction pattern shows the long streaks (diffuse scattering in reciprocal space).
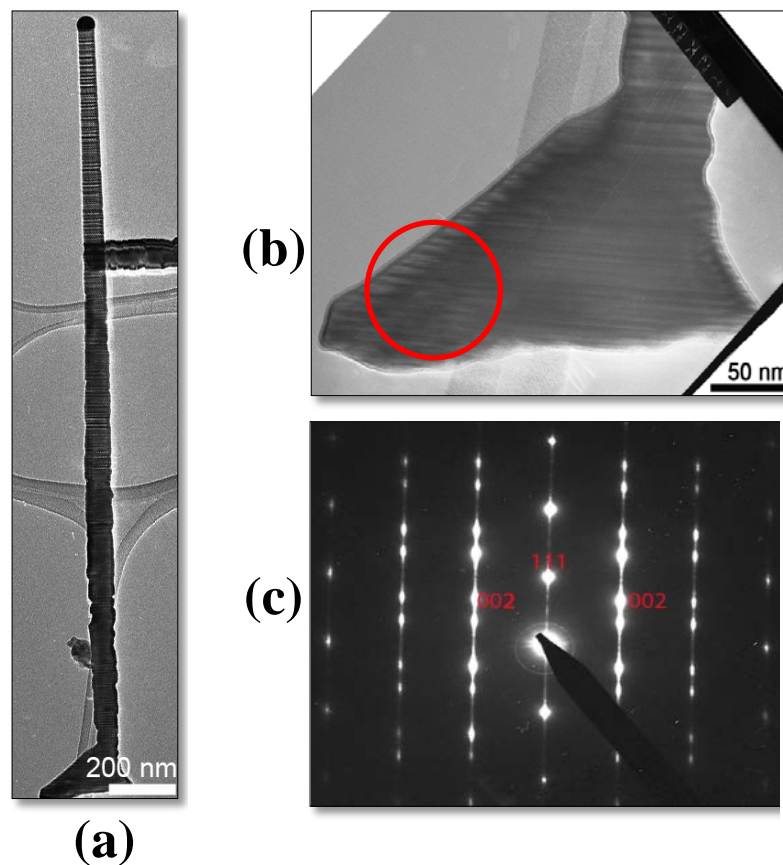
Figure 32: (a) BF image of NW along with substrate. (b) High resolution BF image of NW substrate-interface. (c) SAD pattern from the NW substrate-interface confirmed as ZB with twinning. (Red circle in figure (c) the place where SAD pattern taken).

4.3 Nanowire batch III (SC-95)

Figure 33 an overview image of TEM BF image of Be doped GaAs NW group cleaved along with substrate grown on Si (111) by Ga assisted VLS techniques. The wires are very long, rod shaped almost same diameter but varying in length. In Figure 33 we cannot clearly see the NW substrate interface due to some contamination, so in Figure 36(a) we can clearly see the NW substrate-interface. Since this NW is Ga-assisted, Ga droplet can be seen at the top of the wire which is parallel to the substrate. We can also see some defects and droplets are missing in some of the NWs.
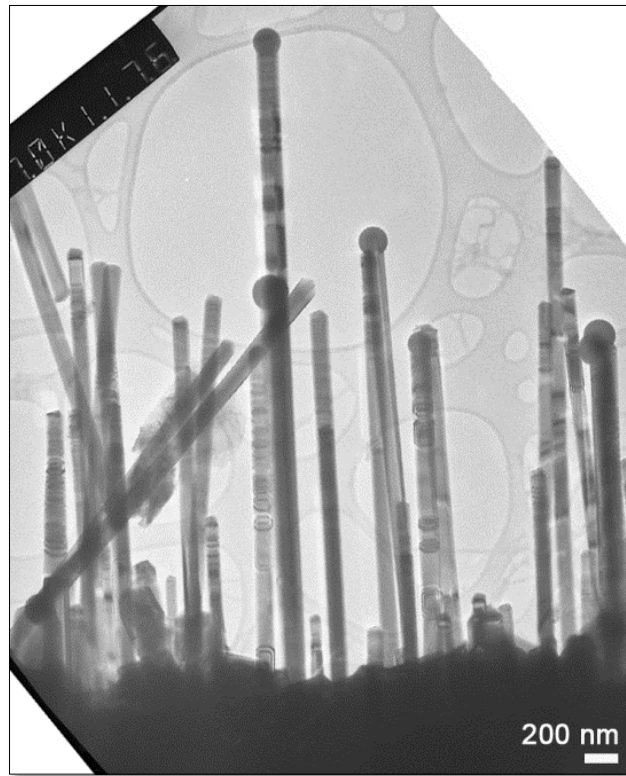
Figure 33*: BF overview image of NW group along with substrate from batch III.*

Figure34 an overview TEM BF image of Be doped GaAs NWs grown by Ga assisted VLS techniques, the wire is vertical and rod shaped with even in diameter from top to bottom with few stacking faults. The Ga droplet looks almost like a circle located at the top of the nanowire which is parallel along with the nanowire. Figure33 (b), (c), and (d) shows the indexed diffraction pattern from the top, middle and bottom parts of the BF nanowire, from the SAD pattern the crystal structure of Be-doped GaAs NW grown by Ga-assisted technique can be predominantly ZB crystal structure with twin and the very bottom part is twin free ZB in [111] NW growth direction.
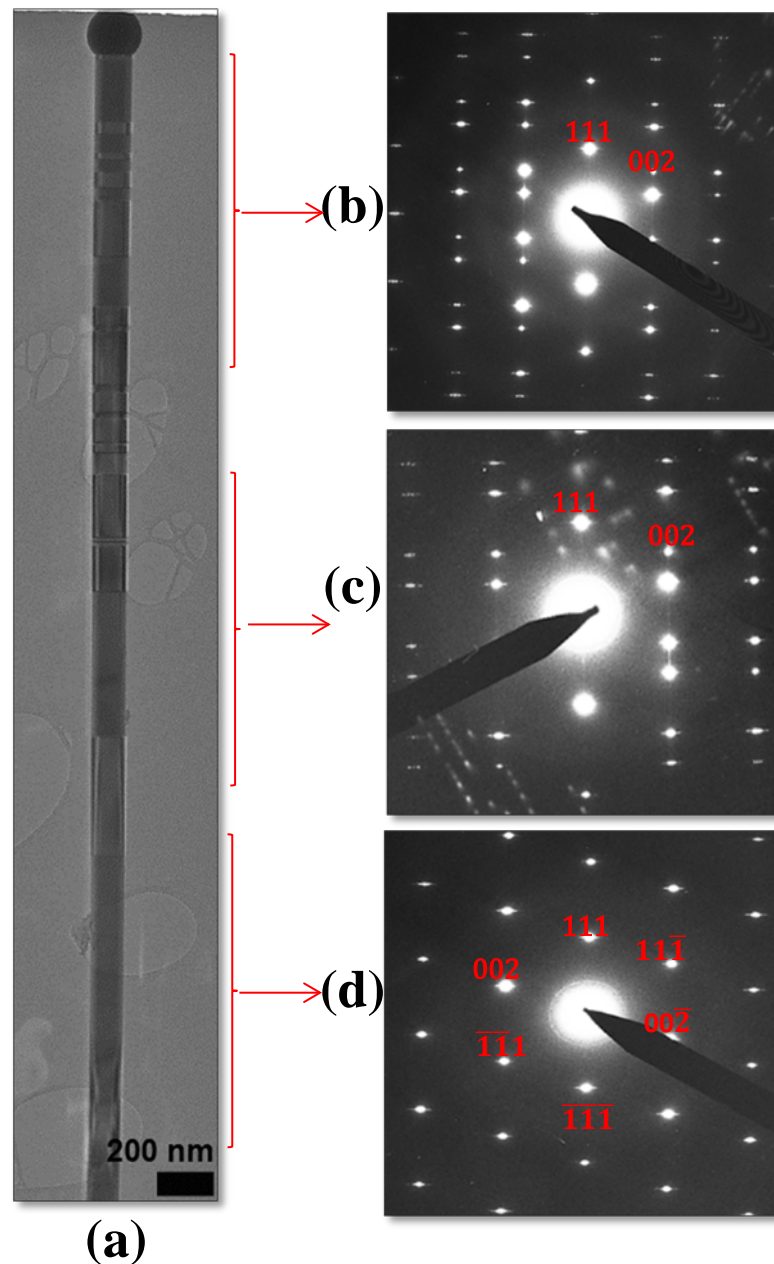
Figure 34: (a) BF image of NW from batch III. (b), (c) and (d) corresponding SAD pattern from top, middle and bottom respectively are predominantly ZB crystal structure. (b) and (c) ZB with twins and (d) twin free ZB.

Figure 35 shows a clear view of BF NW image from NW batch III and clearly seen the twin defects. Figure35 (a) top part of the NW with Ga droplet and few SFs. We can see a clear thickness fringes in the thinner region figure 35(b) middle part of the NW that is at the edge and becomes less visible when it reaches the thicker region of the specimen. Thickness fringes are mostly observed in wedge shaped TEM specimens, so that we can see a set of alternating bright and dark bands. We can observe thickness fringes in the thinner region of the specimen and becomes less visible when it reaches the thicker region of the specimen. This means that intensity between bright and dark bands varying at the thinner and thicker region of the sample. Figure 35(c) the very bottom part and SFs are less.

| (a) | (b) | (c) |
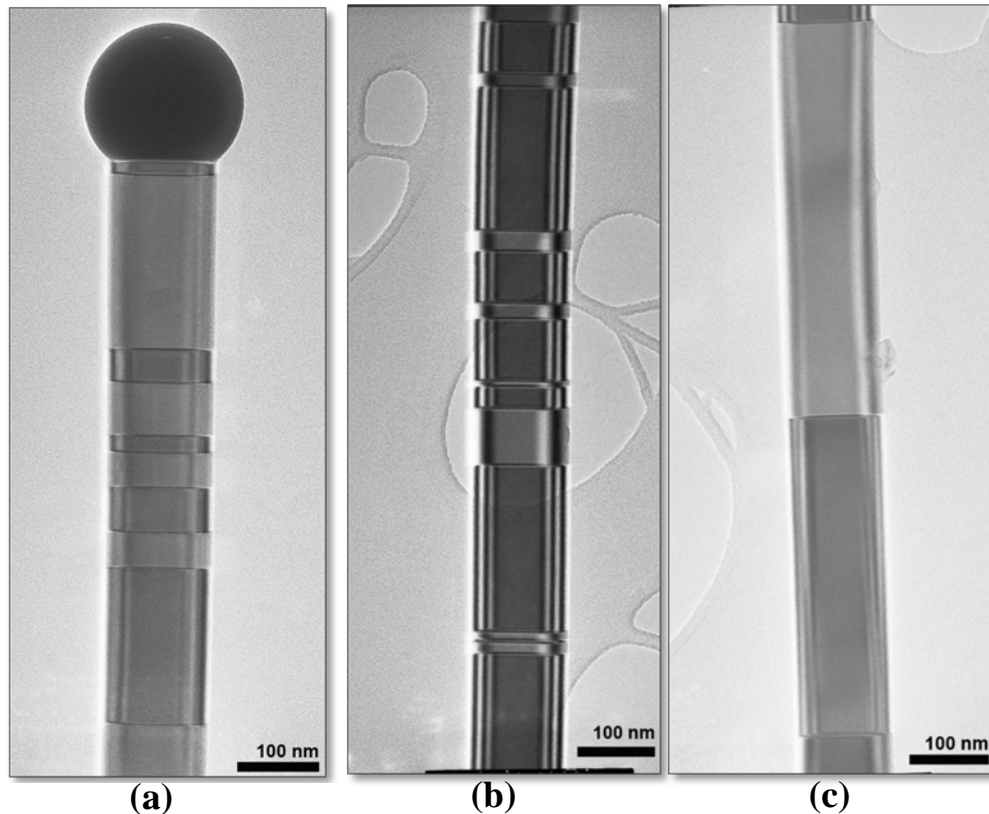
Figure 35: Clear view of BF images from top, middle and bottom part of NW from batch III. (b) Thickness fringes on NW sides, so alternate bright and dark bands can be visible.

Figure 36(a) close up BF images of a cleaved off piece from substrate with NWs attached from batch III. Figure 36 (b) SAD pattern from the substrate interface area is indexed as twin free ZB at [111] growth direction. The stripes seen on the substrate-interface are due to the strain occurs during the sample preparation.

(a)   **(b)**

Figure 36: *(a) BF image from NW substrate interface from batch III. Red circle in figure the place were SAD pattern taken (b) SAD pattern from (a) indexed as twin free ZB at [11$\bar{2}$] zone axis direction.*

4.4 Nanowire batch IV (SC-169)

An overview image of TEM BF image of Be doped GaAs NW group cleaved along with substrate grown by Ga assisted VLS technique is shown in Figure 37. The NWs are varying in length, even in diameter, flat tip and few stacking faults. Figure 37 (b) NWs from the same batch with a different morphology on the top (pencil shaped top) with few SFs.

(a) **(b)**
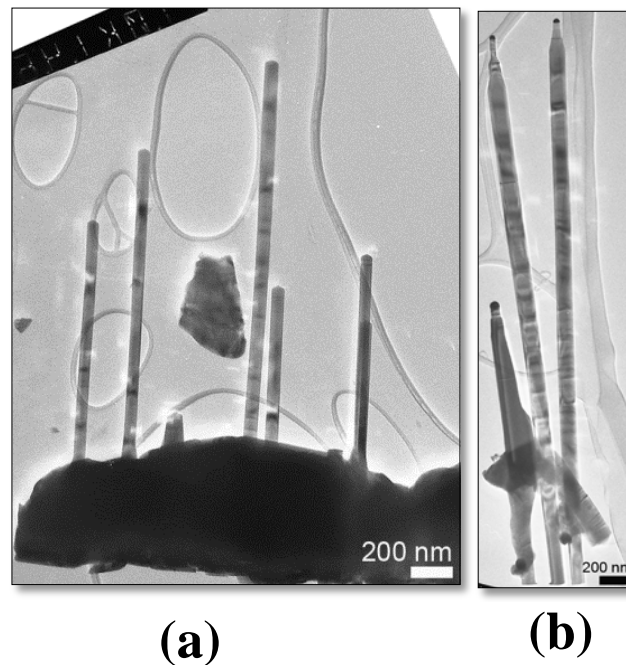
Figure 37: (a) BF overview image of NW group along with substrate from batch IV.(b) Pencil shaped top NWs from the same batch.

Figure 38 (a), (b) and (c) shows the BF images of three NWs from the same batch. Interestingly the shapes of tips are different from each other. In figure38 (a) NW which is vertical, rod-shaped and the tip is almost flat , In figure38 (b) NW which is vertical, rod-shaped with round droplet on top The NW in figure38 (c) looks like a 'walking stick ', a substantial kink at the top of NW (c) and the Ga droplet is not parallel to the NW,. All these

four NWs have very few stacking faults mostly in the top part was observed. The diffraction pattern that observed in detail for all the three NWs are predominantly ZB with twin defects at the top and middle and twin free ZB at the very bottom part in [111] growth direction.
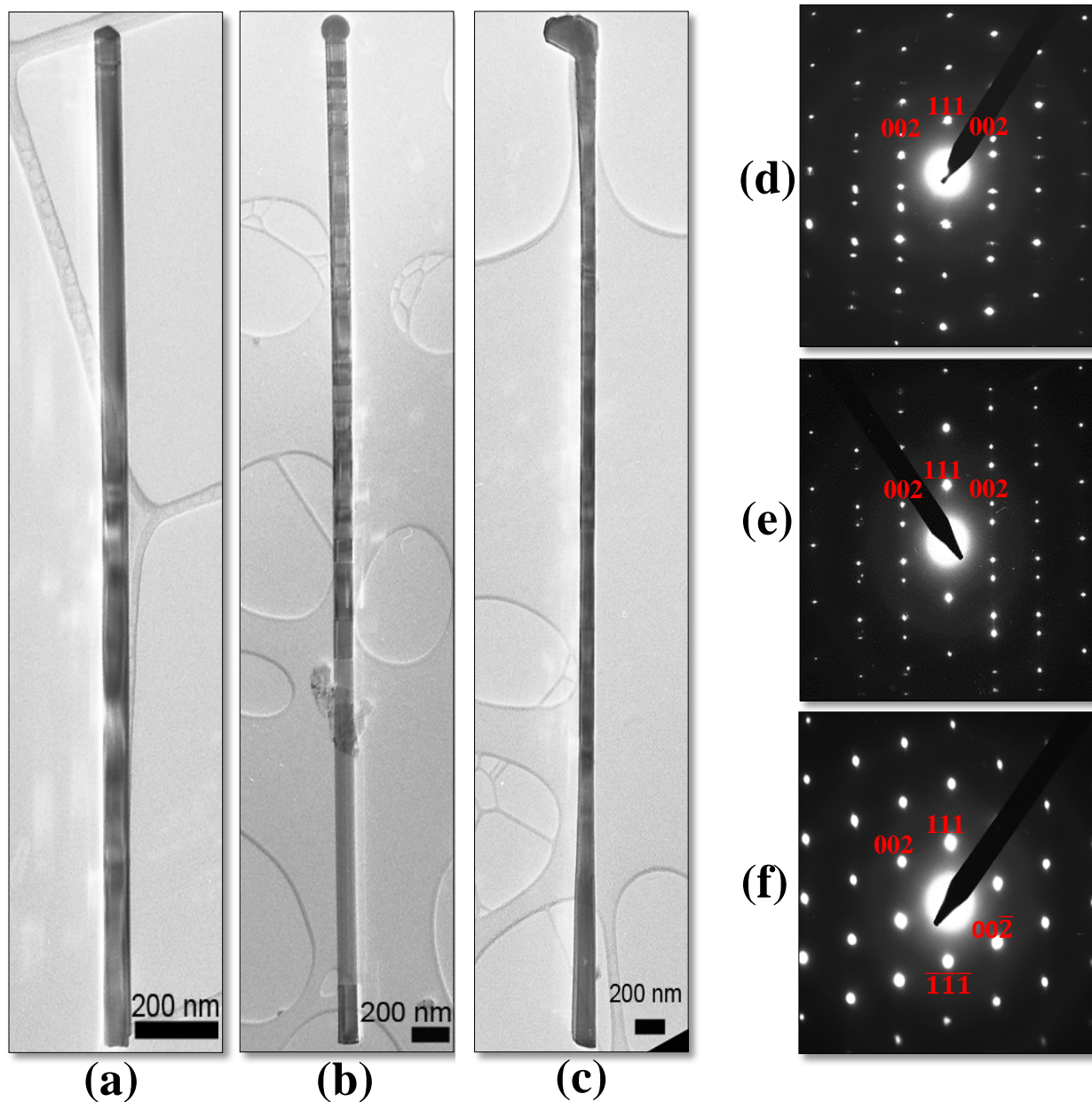
Figure 38: (a),(b) and (c) BF images from three different NWs from batch IV. (d), (e) and (f) SAD patterns from top, middle and bottom part of the NW respectively are indexed as ZB crystal structure. SAD patterns are same in all the three NWs.

Figure 39(a) a cleaved off NW substrate-interface along with three NWs and (b) the corresponding SAD pattern from the NW substrate interface indexed as ZB at [111] growth direction. We can also see some thickness fringe effect dark and bright lines on the side of the substrate.
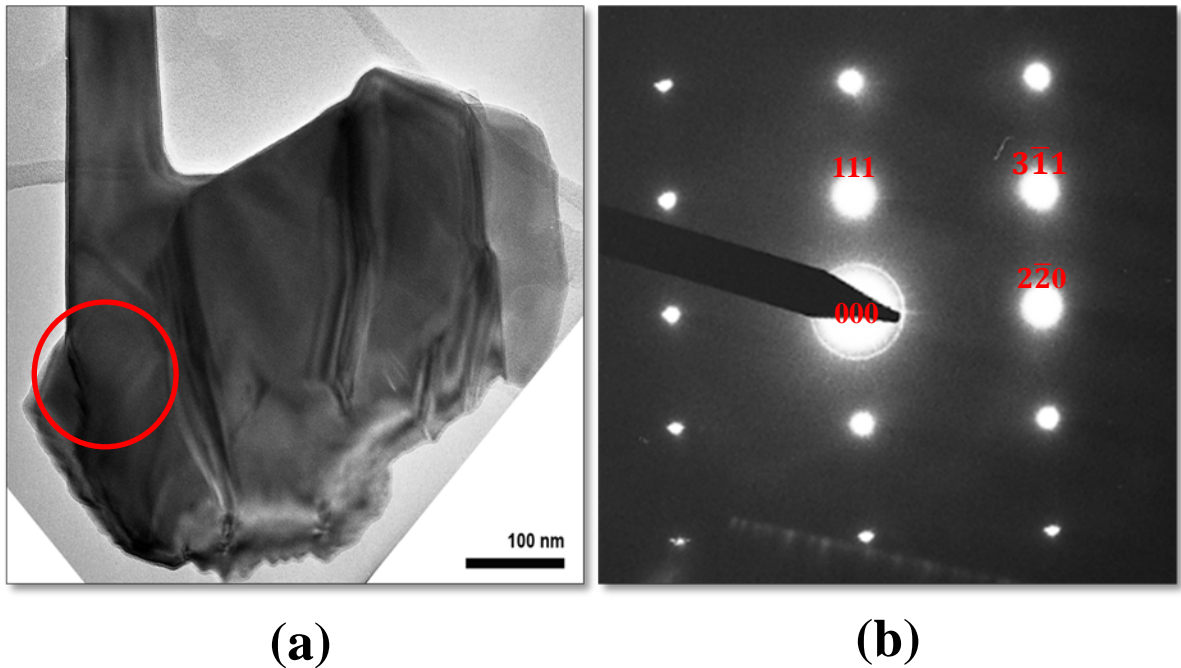

(a)　　　　　　　　　　　**(b)**
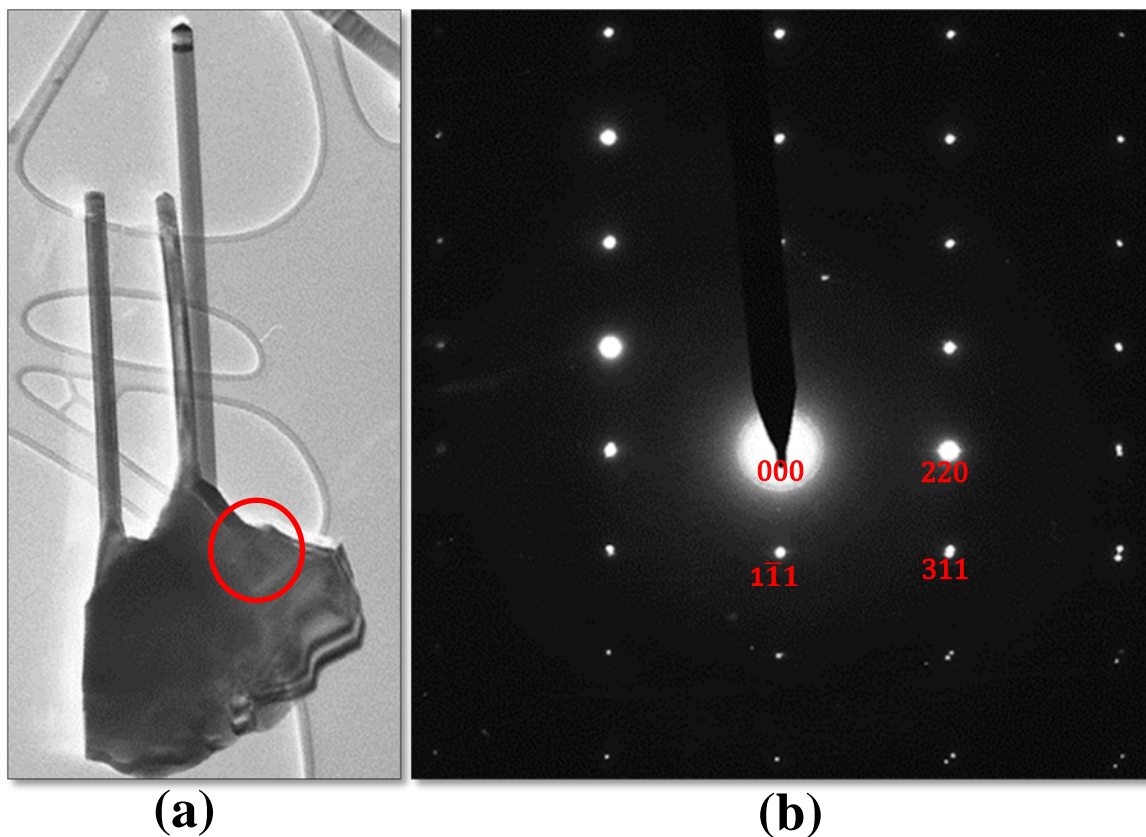
Figure 39: (a) BF image of NW along with substrate from batch IV. Red circle in figure the place were SAD pattern taken (b) SAD pattern from NW substrate interface confirmed by indexing ZB at [111] growth direction.

Chapter 5

Discussion

Control of the doping in semiconductor NWs is essential for constructing a broad range of NW based opto-electronic devices. For GaAs NWs the Ga-assisted VLS technique has recently attracted significant interest due to its potential advantages in the fabrication of core shell structures and the reduced risk of deep levels by exclusion of foreign metal catalyst in the growth process. Both techniques, Au- and Ga-assisted NW generation have their own benefits and drawbacks, due to which understanding the dopant incorporation into the NWs grown by both the techniques is important [17]. To get NW based devices a control doping (low and high) with keeping control on crystal phase, defect density and morphology of NWs are essential. In this section a detailed discussion is carrying out about the effect of Be doping on the structure of Au- and Ga-assisted GaAs NWs on the basis of the results obtained during the course of this study (result figures are shown in chapter 4).

5.1 Effect of doping on NW morphology.

Doping concentration of Be affects the NW morphology in Au-and Ga-assisted GaAs NWs. Detailed discussion is given below.

5.1.1 Au-catalyzed low and high Be doped NWs.

Nanowire batch I (As605-3) is a Be doped GaAs NW grown by Au-assisted MBE at substrate temperature about 510° C. The doping concentration of Be is $8.36x10^{18}cm^{-3}$ was assumed based on the growth parameters, which is low compared to the NW-batch II As-6052. In the overview image figure 23 we can see that there is a slight variation in height and diameter of the NWs. BF images Figure 24(a) & (b) of two different NWs from the same batch, the wires are vertical, rod-shaped with even in diameter and hardly any stacking faults seen in the thicker NW, but few SFs (not morphology but crystal phase) can be observed in the top of the thinner NW.

In the case of **Nanowire batch II (As605-2)** the doping concentration of Be $1.2 x 10^{19} cm^{-3}$ was assumed comparatively very higher than the NW batch I. This NW is extremely different from all the other NWs studied here. The wires seem to be thicker at the bottom and decrease in the diameter when it growing to the top (figure 28). According to the NW morphology, randomly distributed high density stacking faults from bottom to top and the twin planes have both uniform and non-uniform spacing. In addition to these, highly anisotropic overgrowth can be observed on the NW side facets in (111) B direction. The additional overgrowth seems to be less when the diameter of the NW changes from bottom to top, this means that the additional overgrowth is very high in the NW bottom part. Tapering is due to more growth on the NW side facets is very high in this batch.

The additional overgrowth is very high in the bottom part of NW batch II, which could be due to that the bottom part of the NW side facets are exposed to the Ga- and As- flux for longer duration than the lately grown top part of the NW side facets. The high Be concentration affects the shape of the NW. When the doping concentration of Be is increased the NW get high twinning density, exhibits a very remarkable tapered shape due to the nucleation of the NW side walls. But in some part of the NW after a systematic TEM investigation we observed the twin planes that have constant spacing within the NW forming twinning super lattice (TSL) and the very bottom part in all the NWs are randomly distributed very high density of stacking faults. TSL is formed when the (111)A and (111)B (shown in figure 29 b & c) side facets which are not parallel are tilted 54^{0} in opposite directions with respect to the NW axis. The schematic representation of the formation of TSL is shown in figure (31)[10] During growth after a certain moment the top surface of the NW is a hexagon and the shape of the NW droplet is almost spherical. When the NW grows the (111) A side facet move inward with increase in length at the same time the (111) B facet move outward with decrease in length. This distorts the droplet so as to minimize its surface area and leaning towards the (111) A side forms a triangle like shape at the NW-droplet interface. After a certain point this becomes more favorable to form a twin plane which reduces the distortion of the catalyst particle by re-growth towards the hexagonal shape and the process is repeated by producing periodically repeated NWs forms TSL[10]. In addition to form TSL, there is an overgrowth formation on the (111) B facets with high density of twins is because of the high Be doping concentration.
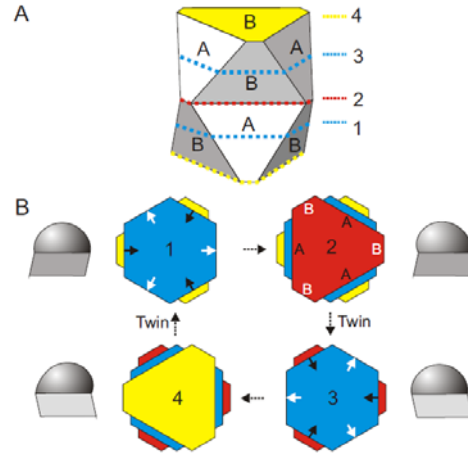
Figure: 40.. (A) Model for TSL[10] in NWs with ZB crystal structure with nonparallel {111} side facets. In figure.40.(B) The cross-sectional shapes of the top facet of the NW at the solid-liquid interface during growth. Owing to the nonparallel orientation of the side facets, (111)A edges increase and (111)B edges decrease in length during vertical growth, as a result a hexagonal interface develops into a triangle like shape. At certain moment, it is energetically more favorable to create a twin plane rather than continue growing towards fully triangular top interface. After twin formation, triangular shape evolves back to hexagonal shape and the cycle is repeated.

According to the VLS growth model proposed by Dubroviskii and Sibirev[18], the most predominant Ga adatom diffusion paths favoring the growth of the NWs by MBE were considered to be (a) diffusion of Ga adatoms on the substrate surface to the NW base and (b) diffusion of Ga adatoms from the NW base to the Au droplet along the NW side walls. Part of the Ga adatoms diffusing on the substrate could contribute to the growth of a 2D layer on the (111)B surface and part of the Ga adatoms diffusing along the NW sidewalls contribute to the radial growth of the NW, overgrowth on NW (111)B side facets.

Doping concentration of Be affects the shape (morphology) of the Au-assisted NW only for the highest applied Be doping concentration. In the case of NW batch I Be doping concentration cannot affect that much in the morphology, very few SFs observed in the thin NWs from the same batch. So if we can control the Be doping concentration to less than $8.36x10^{18}cm^{-3}$ we expect a defect free NW for making them promising for nano scale

devices. In order to make control devices, a high doping without change in morphology is needed.

5.1.2 Ga-catalyzed low and high Be doped NWs.

Nanowire batch III (SC-95) is a Be doped GaAs NW grown by Ga-assisted MBE at substrate temperature about 640°C grown on Si (111) substrate. The doping concentration of Be is $3.5 x 10^{18} cm^{-3}$ was assumed which is low compared to the NW-batch IV SC-169. The NWs are rod shaped with a head on its top, almost same diameter but varying in length with few SFs. In this batch all the NW tips are of same shape most of them with droplet and some are without droplet figure 34(a).

Nanowire batch IV (SC-169) is a Be doped GaAs NW grown by Ga-assisted MBE at substrate temperature about 640^0C grown on Si (111) substrate. The doping concentration of Be is $1.17 x 10^{19} cm^{-3}$ was assumed which is very high compared to the NW-batch IV SC-169. Under a systematic TEM investigation a tremendous difference in the morphology was observed in different single NWs in the same batch (figure 38). NWs grown under high Be doping concentration tend to develop different NW morphology in the top with respect to each other. Different NW morphology includes rod shaped with round tip, rod shaped without droplet, walking stick handle (kinked neck), pencil shaped etc.

In our experimental conditions, though with Be doping we obtained NWs with same morphology as the one without doping as reported in an earlier study. We can conclude from this observation that a low Be doping may not significantly affect the NW morphology. But NWs grown under high Be doping concentration tend to develop different NW morphology with respect to each other. In figure 38(a) the NW is very straight and very few SFs observed So if we can control Be doping during growth we may obtain defect free straight rod-shaped NWs which may be a good candidate for NW based devices. A high doping without change in morphology is required for control NW-based devices.

5.2 Crystal structure and defects.

In this study to identify the defects and crystal structure in NWs, conventional BF and DF TEM imaging along [110] zone axis in combination with SAD and lattice imaging were

applied. Different NWs from all batches were screened in detail for twin defects and SFs over their entire length. The structural defects are thought to be highly detrimental to the realization of future high-performance NW devices.

5.2.1 Au-catalyzed low and high Be doped NWs.

In *Nanowire batch I (As605-3)* where the Be doping concentration is low, the BF images from the thicker NW is observed as defect free whereas the thinner NWs from the same batch seems to have very few SFs near the NW-Au catalyst interface. From the SAD patterns the crystal structure of low Be doped GaAs NWs grown by Au-assisted technique is ZB in [111] growth direction. In thinner NWs the SF is free upto a certain length, after which SFs appear and continues until the Au catalyst/NW interface with some variation in their density or terminates after some length, after a systematic TEM investigation (shown by arrow in figure 24 (a)). Thinner NWs usually grow faster and thicker, NWs usually grow slower when using Au-assisted MBE [19]. Based on this fact and observations that are made here, thinner NWs have SFs than the thicker NWs and this indicates that the density of the SFs depends on the growth rate of the NW. The structural quality of NWs is very important for the performance of NW based devices. Here in this batch material quality is obtained in the thicker NWs than the thinner ones. So it may be a good candidate for NW based devices.

In *Nanowire batch II (As605-2)* where the doping concentration of Be is very high than batch I. NW having very high density of rotational twins with randomly distributed stacking faults and additional overgrowth on NW side facets. From the SAD pattern of the NWs shows that the crystal structure of the NWs is ZB. In this NW we observed very high density of twinning in the NW direction and the overgrowth on the NW side facets also have twinning in the (111) B direction. The SAD pattern from the thick bottom part has extra spots in addition to the normal ZB twinnig spots (red circle in figure 29 (g)) is because of the reflection of planes from different [111] directions both from the NW itself and the overgrowth part on the NW side facets. High Be doping affects the NW crystal structure. When sufficient Be is added to the system the NWs precipitate twinned ZB crystal structure.

The electronic band structure of materials depends on their crystal phase whether the crystal structure is ZB or other. In the case of randomly distributed rotational twins and TSL as we observed in NW batch II, the rotation of the crystal structure may have strong effect as the symmetry of the crystal is varying. These SFs breaks the symmetry of the crystal and act as scattering centres for electrons and holes. The presense of twin planes and SFs may therefore have a significant influence on the electron transport through the NWs[20].

To make NW based device applications, which requires a very precise control of the NWs composition and a perfection of the crystal structure. To understand the formation of these defects and crystal phases and find the ways to reduce the defect density and purify the crystal phases is a challenging problem for III-V NWs.

5.2.2 Ga-catalyzed low and high Be doped NWs.

In *Nanowire batch III (SC-95)* figure 34(a) shows the typical TEM BF image and the corresponding diffraction pattern from the top, middle and bottom respectively. The SAD patterns in figure 34(c) and (b) shows additional spots related to the presence of twinned ZB segments. Under TEM investigation of the full length of several NWs, twin-free ZB segments were observed only at the bottom part of the NW. G. E. Cirlin *et al* [21] reported that, undoped GaAs NWs grown by the Ga- assisted technique have predominantly ZB crystal structure with few twin defects. From these observations we can conclude that a very low Be doping concentration does not have any influence on their crystal structure. It is very clear that within the assumed Be concentration there is no significant difference in either growth rate or crystal structure is observed in between these undoped and very low Be-doped GaAs NWs grown under identical conditions.

In *Nanowire batch IV (SC-169)* from the indexed SAD pattern the diffraction spots can be indexed as ZB crystal structure. Same like SC-95 these NWs have twin free ZB segment was observed in the very bottom part. The high Be doping concentration affects only the morphology not in the crystal structure when compared with NW batch III SC-95. From our study whether the NWs are doped or undoped, the structure of NW crystal structure

seems comparable. An application of NW needs a precise control of the NW composition and perfection of their crystal structure.

5.3 Effect of doping dependent change in NW droplets in Au and Ga catalyzed low and high Be doped NWs.

There is an observed doping dependent change in the size of the NW droplets .By investigating the catalyst particle using TEM in NW batch II with high Be doping concentration, it was found that there is a catalyst inside the droplet (red arrow in figure 27 (b)). In NW batch IV NWs grown under high Be doping concentration tend to develop the formation of different NW tips with respect to each other (figure 38). Different tips like flat tip, round shaped, kinked neck, pencil shaped etc. From the studies of (Mazid *et al* [22]) there is also a direct relation between the crystal structure of the NW and the droplet contact angle whether it is small or high. Here in this study may be both the Be doping concentration and the value of the contact angle influences the shape of the NW droplets.

5.4 Crystal structure study in the NW substrate interface in Au and Ga catalyzed low and high Be doped NWs.

For the structural characterization of NW substrate interface micro cleavage sample preparation method was used to get the NW along with the substrate. The importance of this study is to understand the crystal phase at the NW substrate interface during the initial stage of the NW growth on GaAs and Si substrate. Both the GaAs and Si have cubic Bravais lattice. From all the obtained SAD pattern result from the NW substrate-interfaces are predominantly ZB crystal structures. In figure 32 (b) we can see twinned plane on the NW substrate-interface region and the density of twinning seems to be high at the NW batch II the one with high Be doping concentration grown on GaAs substrate. Because of the spacing between the twinning layer is too small, streaks can be observed in the SAD pattern figure 32(c). In both the Nanowire batch I and II the twinned ZB crystal structure at [111] NW growth direction was observed. This means that the lattice experience a twinning in the NW substrate-interface. Whereas the NWs grown on Si substrate, the SAD patterns were indexed as twin free ZB in [111] NW growth direction. This means that the lattice

cannot have any twinning on the NW substrate-interface. For making NW based device applications the study of NW substrate interface is necessary.

5 5 *Comparison of Au-catalyzed Vs Ga-catalyzed low and high Be doped NWs.*

5.5.1 Morphology.

In the Au assisted low and high a significant change were observed in the morphology of the NWs. NWs with low Be doping concentration are grown axially and are rod shaped with very few defects. Whereas the NWs with very high Be doping are tapered shape due to the nucleation of the NW side walls with high twinning density all over the NW. The very bottom part is highly tapered with randomly distributed twinning and in some parts we observed periodic twinning with overgrowth on the NW side facets in the (111) B direction. In conclusion we synthesized Be doped GaAs NWs by MBE and observed a significant doping dependent change in the NW morphology mainly for highest applied Be doping concentration.

In Ga-assisted a very low Be doping concentration no significant difference in morphology is observed between doped and undoped GaAs grown under identical conditions. But Be doped GaAs NWs by MBE and observed a doping dependent change in the NW morphology only for the highest applied Be doping concentration in Ga-assisted NWs. In the Ga-assisted both the NWs from the two batches are rod shaped and especially NWs grown under high Be doping concentration tend to develop different NW morphology in the top with respect to each other. Different NW morphology includes rod shaped with round tip, rod shaped without droplet, walking stick (kinked neck), pencil shaped etc.

In order to make control devices, a high doping without change in morphology is needed. During growth high Be doping concentration pushes more Ga into the system also a reason for high twinning density and should be studied in more detail to optimize the morphology and purity of the crystal structure. Also regular twinning in NW could be explored further.

5.5.2 Crystal phase.

It has been a challenge to control the crystal phase in Au-assisted growth of III-V NWs due to the fact that III-V NWs, for example GaAs normally adapt a WZ crystal phase with SFs easily rather than the ZB phase [19]. But here in this Au-assisted NW batches grown on GaAs substrate, the doping concentration of Be leads to ZB crystal structure with few twin defects mostly in the thinner NWs in batch I and high density of twinning in NW batch II were observed. From these observations we can conclude that the doping concentration of Be in Au- assisted GaAs NWs has a clear influence on their crystal structure. In the case of Ga-assisted NW batches on Si substrate are ZB with and without twin crystal structure were observed. Applications of NW need a precise control of the NW composition and perfection of their crystal structure.

Diagrammatic representations of all the four NW batches according to morphology and black stripes across the NWs represents density of SFs are shown below.
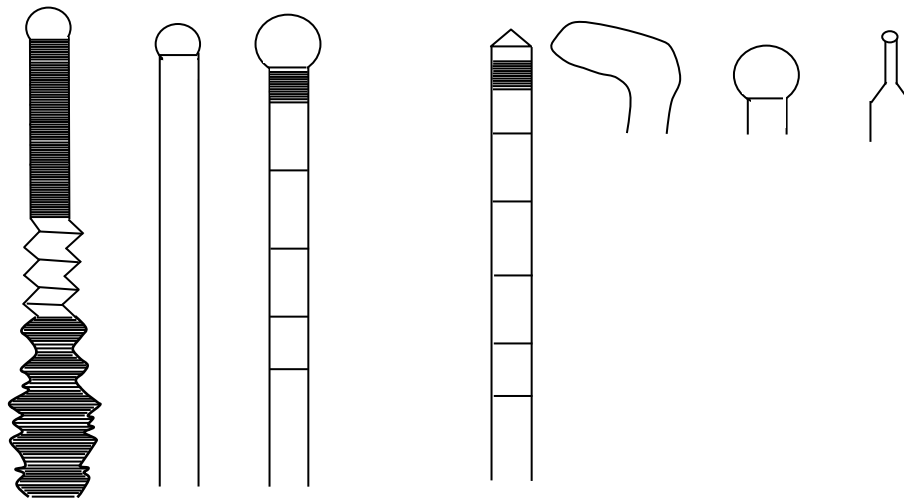

Figure 41 *Diagrammatic representation showing the morphology and SF density of NW batch II, I, III and IV respectively. The additional three NW tops represents the different NW top from NW batch IV.*

Chapter 6

Conclusion

In this study the focus was on Be doping in both Au catalyzed and Ga catalyzed NWs. In addition to the growth of NWs on the substrate surfaces, NW substrate-interface on GaAs (111) B and Si (111) respectively were also investigated and compared by TEM. The effect of doping on the crystal structure and morphology can affect NW-device manufacturing and hence that were also examined.

• ***Nanowire batch I (As605-3)*** is a Be doped GaAs NW grown by Au-assisted MBE at substrate temperature about 510° C. The doping concentration of Be is $8.36x10^{18}cm^{-3}$ based on growth parameters. The wires are vertical, rod-shaped with even in diameter and hardly any stacking faults seen in the thicker NW, but few SFs can be observed in the top of the thinner NW. From the SAD patterns the crystal structure of low Be doped GaAs NWs grown by Au-assisted technique is ZB in $[11\bar{2}]$ zone axis direction. The observed crystal phase at the NW substrate-interface is ZB with twinning.

• ***Nanowire batch II (As605-2)*** Be doped GaAs NW grown by Au-assisted MBE at a substrate temperature about 510° C. The doping concentration of Be is $1.2x10^{19}cm^{-3}$ was assumed comparatively which was very higher than the NW batch I. Upon analysis of NW morphology, tapered shape, randomly distributed high density stacking faults from bottom to top and twin planes having both uniform and non-uniform spacing were observed. Periodically repeated NWs forms TSL and in addition to form TSL, there is an overgrowth formation on the (111) B facets with high density of twins is because of the high Be doping concentration. From the SAD pattern of the NW and the NW substrate-interface shows that the crystal structure is predominantly ZB with twinning.

• Compared with Au-assisted ***Nanowire batch I (As605-3)*** and ***Nanowire batch II (As605-2)*** doping concentration of Be affects the shape (morphology) of the NW only for the highest applied Be doping concentration. In the case of NW batch I, Be doping concentration did not affect that much in NW morphology, very few SFs observed in the

thin NWs from the same batch. So if we can control the Be doping concentration to less than $8.36x10^{18}cm^{-3}$ we expect a defect free NW for making them promising for nano scale devices. In order to make control devices, a high doping without change in morphology and crystal phase is needed.

• *Nanowire batch III (SC-95)* is a Be doped GaAs NW grown by Ga-assisted MBE at substrate temperature about 640°C grown on Si (111) substrate. The doping concentration of Be is $3.5x10^{18}cm^{-3}$. The NWs are rod-shaped almost same diameter but varying in length with few SFs were observed. From the SAD pattern the crystal structure of the NW is ZB twinning in the top and the middle part of the NW and the bottom part is pure ZB. The diffraction pattern from the NW substrate-interface is ZB without twinning.

• *Nanowire batch IV (SC-169)* is a Be doped GaAs NW grown by Ga-assisted MBE at substrate temperature about 640°C grown on Si (111) substrate. The doping concentration of Be is $1.17x10^{19}cm^{-3}$ was assumed, which is very high compared to the NW-batch IV SC-169. NWs grown under high Be doping concentration tend to develop different NW morphology in the top with respect to each other. Different NW morphology includes rod shaped with round tip, rod shaped without droplet, walking stick handle (kinked neck), pencil shaped etc. In figure 38(a) the NW is very straight and very few SFs observed So if we can control Be doping less than $1.17x10^{19}cm^{-3}$ during growth we may obtain defect free straight rod-shaped NWs which may be a good candidate for NW based devices From the SAD pattern the crystal structure of the NW is ZB twinning in the top and the middle part of the NW and the bottom part is pure ZB. The diffraction pattern from the NW substrate-interface is ZB without twinning.

• Compared with Ga assisted *Nanowire batch III (SC-95)* and *Nanowire batch IV (SC-169)* in our experimental conditions, though with Be doping we obtained NWs with same morphology as the one without doping as reported in an earlier study. We can conclude from this observation that a low Be doping may not significantly affect the NW morphology. But NWs grown under high Be doping concentration tend to develop different NW morphology with respect to each other. A high doping without change in morphology and crystal phase is required for control NW-based devices.

In conclusion, we synthesized Be doped GaAs NWs by MBE and characterized them using TEM. We observed a significant doping dependent change in the NW morphology mainly for highest applied Be doping concentration. From our current observations we see that the doping concentration of Be in Au- assisted GaAs NWs has an influence on their crystal structure. We observed the tendency that doping concentration of Be turns all the NWs into ZB crystal phase. In NW batch I the crystal phase is pure ZB but the doping concentration is low. The rest of the three NW batches have ZB with twinning, which is expected to be detrimental for the properties for efficient NW devices. As a whole, our observations depicts that Be doping is affecting the NW morphology and crystal structure. Applications of NW need a precise control of the NW composition, high doping and perfection of the crystal structure. Further research is needed to improve high doping without influencing the crystal structure and morphology of NWs, thereby beneficial for devices based on NWs.

Further work for improving the NW morphology and crystal structure

1. Control Be doping to get periodic twinning.

2. High Be doping pushes more Ga into the system during growth. Reducing the amount of Ga flux and adding sufficient Be into the NW may reduce the crystal defects and achieve TSL structure.

3. Changing the substrate, using Si substrate for Au assisted GaAs-Be NWs and GaAs substrate for Ga- assisted GaAs-Be NWs may be optional.

4. From this study Au assisted Be doped NWs will be good for NW based device applications, by controlling the doping concentration less than $8.36x10^{18}cm^{-3}$ or Be doping concentration in between $8.36x10^{18}cm^{-3}$ and $1.2x10^{19}cm^{-3}$ during growth we may get defect free and periodically twinned NWs.

5. In the case of Ga assisted it may be good if we can control the Be doping concentration in between $3.5x10^{18}cm^{-3}$ and $1.17x10^{19}cm^{-3}$ during growth we may obtain vertical rod shaped twin free NWs for NW based device applications.

References

1   CaroffP *et al.* Controlled polytypic and twin-plane superlattices in iii-v nanowires. *Nat Nano* **4**, 50-55, (2009).

2   Hilse, M., Ramsteiner, M., Breuer, S., Geelhaar, L. & Riechert, H. Incorporation of the dopants Si and Be into GaAs nanowires. *Applied Physics Letters* **96**, 193104-193104-193103, (2010).

3   Hammond, C. *The Basics of Crystallography and Diffraction*. (OUP Oxford, 2009).

4   Asokamani, R. *Solid State Physics: Principles And Applications*. (Anshan, 2007).

5   Kittel, C. *Introduction to Solid State Physics*. (Wiley, 2004).

6   De Graef, M. *Introduction to Conventional Transmission Electron Microscopy*. (Cambridge University Press, 2003).

7   Singh, J. *Smart Electronic Materials: Fundamentals and Applications*. (Cambridge University Press, 2005).

8   Karlsson, L. S. *Transmission Electron Microscopy of III-V Nanowires and Nanotrees*. (Division of Polymer & Materials Chemistry, Lund University, 2007).

9   Kelly, A. A. & Knowles, K. M. *Crystallography and Crystal Defects*. (Wiley, 2012).

10   Algra, R. E. *et al.* Twinning superlattices in indium phosphide nanowires. *Nature* **456**, 369-372, (2008).

11   Fultz, B. & Howe, J. M. *Transmission Electron Microscopy and Diffractometry of Materials*. (Springer, 2002).

12   Williams, D. B. & Carter, C. B. *Transmission Electron Microscopy: Litteraturliste*. (Springer, 2009).

13   Todorovic, J. *Correlated transmission electron microscopy and micro-photoluminescence studies of GaAs-based heterostructured semiconductor nanowires*. Vol. 2012:319 (Norges teknisk-naturvitenskapelige universitet, 2012).

14   Egerton, R. F. *Physical Principles of Electron Microscopy: An Introduction to TEM, SEM, and AEM*. (Springer, 2005).

15   Dheeraj, D. L. *Growth and structural characterization of III-V nanowires grown by molecular beam epitaxy*. Vol. 2010:190 (Norges teknisk-naturvitenskapelige universitet, 2010).

16   Streetman, B. G. & Banerjee, S. K. *Solid state electronic devices*. (Pearson Prentice Hall, 2006).

17   Dheeraj, D. L. *et al.* Comparison of Be-doped GaAs nanowires grown by Au- and Ga-assisted molecular beam epitaxy. *Journal of Crystal Growth*, 2013

18   Dubrovskii, V. G. & Sibirev, N. V. Growth thermodynamics of nanowires and its application to polytypism of zinc blende III-V nanowires. *Physical Review B* **77**, 035414 (2008).

19   Dheeraj, D. L. *et al.* Controlling crystal phases in GaAs nanowires grown by Au-assisted molecular beam epitaxy. *Nanotechnology* **24**, 015601 (2013).

20   Caroff, P., Bolinsson, J. & Johansson, J. Crystal Phases in III--V Nanowires: From Random Toward Engineered Polytypism.*, IEEE Journal of Selected Topics in Quantum Electronics* **17**, 829-846, (2011).

21   Cirlin, G. E. *et al.* Self-catalyzed, pure zincblende GaAs nanowires grown on Si(111) by molecular beam epitaxy. *Physical Review B* **82**, 035302 (2010).

22   Munshi, A. M. *et al.* Crystal phase engineering in self-catalyzed GaAs and GaAs/GaAsSb nanowires grown on Si(111). *Journal of Crystal Growth* **372**, 163-169, (2013).

23   Solberg, J. K. Innføring I Transmission Electron Mikroskopi compendium.

Appendix

(i)   Method for indexing the Diffraction Patterns.

This is a method for determining the crystallographic data from the specimen. When a diffraction pattern is observed on the viewing screen of the TEM, it is located at a distance L from the specimen. This distance is called the camera length, a fictious length depending on the strength of the lenses. We can increase the magnitude of the diffraction pattern by increasing Land its value is shown on the microscope display. When the Bragg condition is fulfilled, the electron beam will be reflected from the specimen's crystallographic planes, to form diffraction spots on the viewing screen. See the figure 41 below.
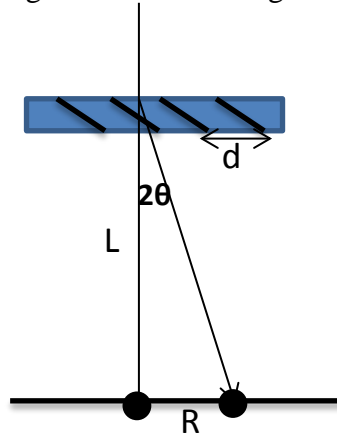

Figure 41: *Relationship between the camera length L, R distance from central spot to nearest diffraction spot and Bragg's angle θ* [23]

From figure; $tan2\theta = \frac{R}{L}$

θ is small, $tan2\theta = 2tan\theta = 2sin\theta$

$\therefore 2sin\theta = \frac{R}{L}$

From Braggs law; $2dsin\theta = \lambda$ or $2sin\theta = \frac{\lambda}{d}$

Combining two equations we get;

$\frac{R}{L} = \frac{\lambda}{d}$ or $Rd = \lambda L$ or $Rd = k$; where $k = \lambda L$

λ is the wavelength of the electron and d is the lattice plane spacing. For different R values for example;

$$R_1 = \frac{k}{d_{h_1 k_1 l_1}} \quad \text{And} \quad R_2 = \frac{k}{d_{h_2 k_2 l_2}}$$

$$\frac{R_1}{R_2} = \frac{d_{h_2 k_2 l_2}}{d_{h_1 k_1 l_1}} = \frac{\frac{a}{\sqrt{h_2^2 + k_2^2 + l_2^2}}}{\frac{a}{\sqrt{h_1^2 + k_1^2 + l_1^2}}} \quad \text{or} \quad \frac{R_1}{R_2} = \frac{\sqrt{h_1^2 + k_1^2 + l_1^2}}{\sqrt{h_2^2 + k_2^2 + l_2^2}}$$

The angle between the corresponding vectors with (000) as the origin is given by;

$$cos\theta = \frac{h_1 h_2 + k_1 k_2 + l_1 l_2}{\sqrt{h_1^2 + k_1^2 + l_1^2}\sqrt{h_2^2 + k_2^2 + l_2^2}}$$

We can label the individual diffraction spots with their corresponding values of h, k and l. Indexing starts by identifying the brightest spot in the center of the diffraction (000) and also index two independent diffraction spots near the (000)spot. The following are the steps for indexing the diffraction pattern from a crystal.

1. Measure several R values for plane distances d and measure the angles between different reflections (angles between lattice planes).

2. Calculate the ratios between the lengths, for example $\frac{R_1}{R_2}$

3. Compare with the table of such ratios to find the family of planes.

4. Measure the angle by trial and error and we find the accurate indices that satisfies the equation

$$cos\theta = \frac{h_1 h_2 + k_1 k_2 + l_1 l_2}{\sqrt{h_1^2 + k_1^2 + l_1^2}\sqrt{h_2^2 + k_2^2 + l_2^2}}.$$

5. Index the rest of the reflections by vector addition and compare the indexed reflections matches with length ratios and measured angles.

After complete the indexing of a diffraction pattern, we need to find the normal to the plane of the diffraction pattern. This normal is called the zone axis and is pointing towards the electron gun in most TEM. This can be calculated by simply taking the cross products of linearly independent vectors for example;

$$[h_1 k_1 l_1] X [h_2 k_2 l_2] = \begin{bmatrix} x & y & z \\ h_1 & k_1 & l_1 \\ h_2 & k_2 & l_2 \end{bmatrix} = [(k_1 l_2 - l_1 k_2), (h_1 l_2 - l_1 h_2), (h_1 k_2 - k_1 h_2)$$

And this is the vector that is vertical to the microscope, normal to the specimen surface.

(ii)   TEM alignment

Mounting the Specimen.

Mount the specimen in a double tilt holder and check the specimen-holder under a light microscope to make sure the position of the specimen is mounted properly. Then press the vacuum system ON, wait for the cycle of pumping the buffer tank to finish and insert the Specimen-holder into the TEM specimen chamber and connect the double tilt plug. Before selecting the parameter High tension 200kV, we need to make sure that the Ion Getter Pump (IGP) is at 27 or less. The function of IGP is to allow a chemically reactive surface to absorb or adsorb stray gas atoms. Then the next step is to heat up the filament $L_a B_6$ an ordinary light bulb by turning the filament knob until we see the "cat's eye" on the fluorescent screen.

The gun and condenser alignment.

Select the second largest condenser aperture, concentrate the beam and move it to the center with BEAMSHIFT. By using aperture adjustment screws we can make our beam symmetrically. The condenser system consists of two lenses and two sets of tilt-and-shift double deflection coils, for to change the angle of the incident illumination coming from the condenser lens hits the specimen. The first set of shift and tilt coils are located just below the filament source which aligns the gun with the first condenser lens and the second

set of shift and tilt coils are located just below the second condenser system. In order to reduce the loss of resolution and image distortion we need to well aligned the optical elements. The purpose of selecting the GUN-TILT is to make the beam bright and symmetric by using the Multifunction-xy knobs. Next step is to shift the gun to the center of the screen again by using multifunction xy knobs and also turn up and turn down the spot size to bring back the illumination to the center fluorescent of the screen. The mechanism of the gun shift alignment is that , as the first condenser lens is strengthened, the first cross over moves closer to the optic axis , in this condition we adjusted the beam shift. When the first condenser lens is weakened the first crossover beam moves diagonally away from the optics axis so that we adjusted our gun shift.

Astigmatism

  Every time when we adjust or switch the electron lens, the magnetization of the metal in the lens changes. This means that when our magnetic lens is not perfectly round Astigmatism occurs. So we can correct the condenser stigmatism by selecting the STIG button and making the beam pattern sharp and symmetric by adjusting the Multifunction-xy knobs which controls the condenser stigmators. Then we can carefully saturate the filament until reaches the filament limit. Then select the emission value in between 1-3.

Eucentric height.

  The physical height adjustment which reduces the movement of the image is called Eucentric height. At about 20kx, put a recognizable feature at the center of the fluorescent screen, tilt the goniometer $\pm10\text{-}20_0$ and if the specimen moves , move it back by adjusting the screw on the goniometer. Through this adjustment we can reduce the minimal movement of the image as a function of tilting the specimen holder back and forth .Repeat this for every new location on the specimen.

Pivot points.

  This is the process by which the beam tilt should rotate the beam through a point in the specimen like a pivoting lever movement about a point. Pivot point also depends the height of the specimen, means that whenever we change the specimen height, we need to readjust

the pivot points at every new location in the specimen. When we press the Pivotpoint-xy in the TEM, if the pivot points are wrong we can see two beams separated laterally on the fluorescent screen. We can adjust the two beam co-incidence by using Multifunction-xy knobs and shift to the center of the screen by Beam shift knobs. Then the next step is to minimize the movement of the object, by moving some object to the center of the screen and spread the beam to the edge of the screen, select Rotation-center and Current and minimize the movement by adjusting the Multifunction-xy knobs.

After all the alignments we can use the microscope for different modes of operations such as imaging mode, diffraction mode and so on.